

Transition in elastic Dean flow: the centre-mode versus hoop-stress pathways

P.S.D. Surya Phani Tej¹, Ganesh Subramanian^{2†}, and V. Shankar^{1‡}

¹Department of Chemical Engineering, Indian Institute of Technology, Kanpur-208016, India

²Engineering Mechanics Unit, Jawaharlal Nehru centre for Advanced Scientific Research, Bangalore - 560064, India

We analyse the stability of viscoelastic Dean flow (flow of an elastic fluid through a curved two-dimensional channel, driven by an azimuthal pressure gradient) in the absence of fluid inertia. This configuration is well known to exhibit a hoop-stress-driven ‘purely elastic’ instability (referred to henceforth as the hoop-stress mode – ‘HSM’) on account of the base-flow streamline curvature. The objective of this study is to demonstrate the existence and importance of a distinct elastic instability in this flow configuration, which is not driven by hoop-stresses, but instead is a continuation of a novel ‘centre-mode’ (CM) instability recently identified in rectilinear shear flows. On account of its origins, the CM instability in Dean flow is expected for two-dimensional (azimuthally varying) disturbances with no axial variation, but continues to exist for three-dimensional disturbances. In contrast, the HSM instability is expected primarily in the axisymmetric limit, and again continues to exist for three-dimensional disturbances.

We use both the Oldroyd-B and FENE-P models to map out parameter regimes in the Wi – ϵ – β space where the aforementioned instabilities are present. Here, Wi is a suitably defined Weissenberg number that characterizes fluid elasticity, β is the ratio of solvent to total solution viscosity, and ϵ is the ratio of the gap (channel) width to the radius of curvature. While its origin in rectilinear shearing flows might lead one to expect the CM instability to only be present for small ϵ ’s (the ‘narrow-gap’ limit), we show that it exists even for $O(1)$ values of ϵ , and over a larger range of Wi . Nevertheless, within the Oldroyd-B framework, the HSM determines the stability threshold for experimentally relevant gap-width ratios, corresponding to $0.1 \leq \epsilon \leq 1$, with the CM becoming the most unstable mode only for $\epsilon < 0.001$. For the more accurate FENE-P model, however, decreasing the finite extensibility parameter L has opposing effects on the HSM and CM instabilities – stabilising the former, but destabilising the latter. In the dilute solution regime ($\beta > 0.95$), and for realistic values of $L \sim O(100)$, corresponding to polymer molecular weights of $O(10^5\text{--}10^6)$ g/mol, the CM remains the most unstable mode for $\epsilon \leq 0.25$, rendering it potentially relevant to the onset of elastic turbulence in the flow of such polymer solutions through curved channels.

Key words: Viscoelastic flows; Dean flow; purely-elastic instability, centre-mode.

† Email address for correspondence: sganesh@jncasr.ac.in

‡ Email address for correspondence: vshankar@iitk.ac.in

1. Introduction

Viscoelastic fluids subject to a shearing flow often exhibit strikingly novel instabilities engendered by their elastic nature, and that are absent in their Newtonian counterparts. For instance, it is well known, since the pioneering work of [Larson *et al.* \(1990\)](#), that Taylor-Couette flow of a viscoelastic fluid exhibits a linear instability even when fluid inertia is negligible. Analogous instabilities have been demonstrated for the flow of polymer solutions in other curvilinear geometries such as cone-and-plate flow ([McKinley *et al.* 1991](#)), torsional flow between parallel circular discs ([Byars *et al.* 1994](#)), and the Dean and Taylor-Dean flow configurations ([Joo & Shaqfeh 1991, 1992, 1994](#)). These instabilities, referred to as ‘purely elastic’ instabilities (see [Shaqfeh 1996](#)), rely on two key ingredients in the base state – streamline curvature and a streamwise normal stress that has a tensile character (owing to stretched polymers). The latter results in a ‘hoop stress’ in the aforesaid curvilinear flows that then drives an instability even in the absence of inertial forces; note that the latter forces come into play even in a Newtonian fluid, leading to inertial instabilities beyond a threshold Reynolds number (Re) in the aforementioned configurations. The Pakdel-McKinley (PM) scaling arguments ([Pakdel & McKinley 1996](#); [McKinley *et al.* 1996](#)) provide a unifying expression for the onset of hoop-stress-driven instabilities, given by

$$\frac{\lambda V}{\mathcal{R}} \frac{N_1}{|\tau|} \geq M_{crit}^2, \quad (1.1)$$

where λ is the (longest) relaxation time of the fluid, V is a characteristic velocity scale, \mathcal{R} is the pertinent radius of curvature, N_1 is the first normal stress difference, τ is the total shear stress in the base-state, and M_{crit} is an $O(1)$ number sensitive to the actual geometry. The PM criterion cannot be satisfied for rectilinear shearing flows (with $\mathcal{R} \rightarrow \infty$), implying that hoop-stress-driven linear instabilities are absent in such flows. We note, however, that hoop stresses in these flows can become relevant at a nonlinear order, owing to curvature of the perturbed streamlines, as has been demonstrated within the framework of a weakly nonlinear stability analysis ([Morozov & van Saarloos 2005a, 2007, 2019](#)). The aforesaid absence of a hoop-stress-driven linear instability had led to the viewpoint that purely elastic instabilities are restricted to curvilinear configurations, even if they be more complicated than the canonical geometries above ([Haward *et al.* 2016](#)), and that rectilinear viscoelastic shear flows are therefore linearly stable ([Bertola *et al.* 2003](#); [Pan *et al.* 2013](#)).

In a significant departure from this paradigm, recent work by [Khalid *et al.* \(2021b\)](#) demonstrated that inertialess plane Poiseuille flow of an Oldroyd-B fluid is linearly unstable in the limit of high Weissenberg numbers ($Wi = \lambda V/H \sim 10^3$, V being the base-state maximum speed, and H the channel half-width) and a near-unity solvent to solution viscosity ratio ($\beta > 0.99$); this corresponds to ultra-dilute highly elastic polymer solutions. The unstable mode has a phase speed close to the base-state maximum, belonging therefore to a class of ‘centre modes’, and the instability arises due to a critical-layer mechanism that does not rely on streamline curvature. [Khalid *et al.* \(2021b\)](#) further showed that, with increasing Re , the elastic centre-mode instability smoothly crosses over to the elastoinertial centre-mode instability, predicted in an earlier effort by [Khalid *et al.* \(2021a\)](#). [Kerswell & Page \(2024\)](#) have recently carried out a matched asymptotic expansions analysis to capture this unstable centre mode. Further, [Buza *et al.* \(2022b\)](#) and subsequently [Khalid *et al.* \(2025\)](#), have shown using the FENE-P model, that accounts for finite extensibility of the polymer molecules, that the elastic centre-mode instability is present even for $Wi \sim O(100)$ and $\beta \sim 0.97$. Thus, use of the more realistic FENE-P model extends the unstable domain to experimentally accessible parts of the parameter space.

Recent efforts have identified an unstable centre mode in other rectilinear shearing flows

as well. [Yadav *et al.* \(2024\)](#) have shown that the elastic centre-mode instability is present in the Couette-Poiseuille family (CPF), but only when the base-state velocity profile is non-monotonic, with a maximum within the flow domain; the instability being absent in plane Couette flow, and more generally, in shearing flows with monotonic velocity profiles. This intimate connection between the presence of a base-state maximum, and the existence of a centre-mode instability, is further corroborated by the presence of the latter in viscoelastic Kolmogorov flow ([Kerswell & Page 2024](#); [Lewy & Kerswell 2025](#)); although the significance of this finding was not recognized in the original analysis of [Boffetta *et al.* \(2005\)](#). An analogue of the centre-mode instability was also shown to be present in viscoelastic film flow down an inclined plane ([Priyadarshi *et al.* 2023](#)), with a semi-parabolic base-state velocity profile.

Thus, there are two qualitatively different elastic instabilities that operate in viscoelastic shearing flows: (i) the hoop-stress mode (‘HSM’ henceforth) which requires the presence of streamline curvature, but exists even for monotonic velocity profiles (such as Taylor-Couette flow), and (ii) the elastic centre mode (‘CM’ henceforth) which does not rely on streamline curvature, but requires a non-monotonic base-state velocity profile. This raises the intriguing possibility that these modes might co-exist in flow configurations which possess both the aforementioned ingredients. That is to say, one has the potential for elastic instabilities of different physical origins in the same flow, a possibility that has not yet been explored in the literature. One such configuration is Dean flow – the flow in a curved channel driven by an azimuthal pressure gradient. In the Newtonian context, this configuration was first analysed by [Dean & Chapman \(1928\)](#), who showed the presence of a centrifugal instability. The threshold for this instability, in the narrow-gap limit, can be obtained from an inertial analogue of the PM criterion above, with the Reynolds number Re replacing Wi ; this was indeed pointed out by [McKinley *et al.* \(1996\)](#) while formulating their criterion for elastic instabilities. As alluded to above, [Joo & Shaqfeh \(1991, 1992, 1994\)](#) analysed the viscoelastic Dean flow problem, albeit in the inertialess limit ($Re = 0$), and showed the presence of an HSM instability in this configuration. One could also have a combination of an azimuthal pressure gradient and wall motion driving the flow, the resulting configuration being dubbed the ‘Taylor–Dean’ flow ([Joo & Shaqfeh 1991](#)), and being more easily realized in experiments.

In this study, we carry out a linear stability analysis of viscoelastic Dean flow to explore the relevance of the centre- and hoop-stress modes in a viscoelastic parameter space comprising Wi , β , and the gap-width ratio $\epsilon = d/R$, d being the channel width. For the case where the curved channel is the gap between concentric rotating cylinders with R_2 and R_1 being the outer and inner cylinder radii, as is typically the case in experiments, $d = (R_2 - R_1)$ may be identified with the gap width, and the radius of curvature with R_1 . We consider the inertialess regime in this effort, and therefore, set $Re = 0$. Traditionally, the HSM has been first analysed in the narrow-gap limit ([Larson *et al.* 1990](#); [Joo & Shaqfeh 1991](#)), corresponding to $\epsilon \ll 1$, with this assumption being relaxed in subsequent numerical investigations ([Joo & Shaqfeh 1992, 1994](#)). In the narrow-gap limit, in order for the hoop stress to remain relevant in the leading order radial momentum balance, one requires $\epsilon^{1/2} Wi \sim O(1)$. Here, $Wi = \lambda U_m / d$ is the Weissenberg number based on the gap width d and a velocity scale U_m associated with the Dean flow profile (defined below). Thus, in the narrow-gap limit, the critical Wi for the HSM instability must diverge as $\epsilon^{-1/2}$. In the same limit, the critical Wi for the CM instability is independent of ϵ , and approaches that of plane Poiseuille flow ([Khalid *et al.* 2021a](#)). At a scaling level, therefore, as $\epsilon \rightarrow 0$, the critical Wi for HSM should eventually become larger than that for the CM. However, owing to the relatively large threshold, $Wi \sim O(10^3)$ for the CM (within the Oldroyd-B framework), it is necessary to carry out the stability analysis to determine the precise value of ϵ corresponding to this crossover, and thereby assess its relevance to typical configurations used in experiments and applications. To this

end, we present here a comprehensive account of the parameter regimes in which either of the aforementioned modes is the most unstable in viscoelastic Dean flow, by considering arbitrary gap-width ratios (ϵ), and by including both axisymmetric and non-axisymmetric disturbances.

While the existence of two types of elastic instabilities in the Dean flow configuration is of interest from the fundamental viewpoint, it is also significant from the applications perspective. Viscoelastic Dean flow is often used for hydrodynamic focusing of particles in curved (Nikdoost & Rezai 2020), spiral (Bai *et al.* 2023), and serpentine (Chen *et al.* 2024) microchannels. Although such experiments involve finite Reynolds numbers, the secondary flows emerging from the elastic instabilities reported in this study could certainly impact particle migration, and more generally, the efficiency of focussing protocols on microfluidic platforms. Polymer solutions are also used as displacing agents in enhanced oil recovery, in order to remove capillary entrapments of oil in the pores. In this context, flow in serpentine microfluidic channels has been used to mimic the tortuous nature of the flow in porous media (Shakeri *et al.* 2021), wherein elastic instabilities are harnessed in triggering the breakup of large capillary entrapments and in the eventual removal of the same. Importantly, the elastic turbulence regime accessed in previous experiments involving serpentine microchannels (also regarded as an important means of achieving efficient mixing in microfluidic devices; see Groisman & Steinberg 2001, 2004) is either explicitly or implicitly understood as the eventual consequence of an initial hoop-stress-driven instability. Our findings suggest that there might exist two distinct pathways (viz., an HSM-based route, and a CM-based route, as suggested by the title) to the eventual turbulent regime, and perhaps, even two different kinds of turbulent states, depending on the wavelength of modulation of the serpentine channel.

We consider both the Oldroyd-B and FENE-P constitutive equations to model the viscoelastic fluid. The Oldroyd-B model has the necessary ingredients to capture both HSM and CM, but owing to its prediction of a shear-rate-independent viscosity and first normal stress coefficient, it may be not accurate for fast shearing flows of polymer solutions (translating to a large threshold Wi for the CM in the present context) where shear thinning becomes important. This lacuna is due to the restrictive assumption of the polymer molecule being an infinitely extensible bead-spring dumbbell. The FENE-P model (Bird *et al.* 1980) overcomes this shortcoming by accounting for finite extensibility via the parameter L , the ratio of the fully-extended length of the polymer (dumbbell) to its equilibrium size; the Oldroyd-B model being realized in the limit $L \rightarrow \infty$. The FENE-P model predicts shear thinning of both the viscosity and the first normal stress coefficient, and hence is a more realistic model at higher Wi . As will be shown below, the consideration of finite extensibility is particularly important in the present scenario, on account of its contrasting effects on the HSM and CM instabilities. Well, why then should one consider the Oldroyd-B model at all? As noted by Shaqfeh & Khomami (2021), in their review article commemorating the birth centenary of James Oldroyd, the results obtained using the Oldroyd-B fluid have their own value in terms of providing a base reference, and (we quote) “it is perilous...to ignore the analysis based on the Oldroyd-B model for any elastic flow problem”! Before we proceed with the present work, we provide a brief review of the relevant literature on HSM and CM instabilities.

1.1. *The hoop-stress instability in viscoelastic Dean flow*

Since the focus of this work is on Dean flow, we do not review here the significant progress made in understanding the HSM in viscoelastic Taylor-Couette flow, since its discovery by Larson *et al.* (1990). Despite sharing some similarities, there are many differences vis-à-vis the HSM instabilities in these two flows, and the reader is referred to recent reviews (Datta *et al.* 2022; Shaqfeh & Khomami 2021; Castillo Sánchez *et al.* 2022) for the latest developments in this area. Suffice it to say that this flow configuration still commands signif-

icant interest among researchers, as can be seen from the recent experiments of [Zhang *et al.* \(2025\)](#), who showed that there is a continuous transition between the elastic and elastoinertial turbulent states in Taylor-Couette flow, by probing elasticity numbers ($E = Wi/Re$) ranging over two orders of magnitude. Although a connection between the elastoinertial and elastic turbulent states was first speculated by [Samanta *et al.* \(2013\)](#) in their observations concerning the onset of elastoinertial turbulence in pipe flow of polymer solutions, a demonstration of a connected linearly unstable region, across the entire range of E , was provided by [Khalid *et al.* \(2021a\)](#), in the context of plane Poiseuille flow.

Following the identification of a purely elastic instability in the Taylor-Couette set-up by [Larson *et al.* \(1990\)](#), [Joo & Shaqfeh \(1991, 1994\)](#) first demonstrated, again using the Oldroyd-B model, the presence of an HSM instability in the inertialess flow through a curved planar channel, driven by an azimuthal pressure gradient (the Dean flow configuration), as well as in the Taylor-Dean configuration where there is the added tangential motion of one of the boundaries. The authors assumed axisymmetric disturbances to begin with, and used the narrow-gap limit to show the presence of the hoop-stress instability when $Wi \gtrsim \epsilon^{-1/2}$, ϵ being the gap-width ratio mentioned above; subsequently, the authors explored finite ϵ 's and non-axisymmetric disturbances. They also carried out experiments, wherein a Taylor-Dean flow (with zero net azimuthal flow rate) was realized in the gap between concentric rotating cylinders with an azimuthal obstruction, and found a qualitative (but not quantitative) agreement between the experimental and theoretical thresholds. In contrast to the Taylor-Couette configuration ([Avgousti & Beris 1993](#); [Joo & Shaqfeh 1994](#)), the unstable mode in the Dean configuration is stationary and axisymmetric. Later, [Ramanan *et al.* \(1999\)](#) demonstrated the stabilizing effect of an imposed axial flow on the Dean flow HSM, again focusing on stationary, axisymmetric modes.

The above conclusions for the HSM in Dean flow were arrived at within the Oldroyd-B framework. With the narrow-gap limit in mind, it is natural to enquire as to how these conclusions are modified at higher Wi , using a more accurate nonlinear constitutive model. Over the past decade, several experimental studies ([Dutcher & Muller 2013](#); [Schaefer *et al.* 2018](#); [Lacassagne *et al.* 2021](#); [Steinberg 2021](#); [More *et al.* 2024](#)) have explored elastic instabilities in various curvilinear geometries, in regimes where shear thinning is important, thereby making the case for a nonlinear constitutive model even more compelling. The general expectation is that shear thinning of the first normal stress coefficient, that arises in any nonlinear model, will weaken the elastic stresses that drive the HSM instability. Indeed, the earlier work of [Byars *et al.* \(1994\)](#) and [McKinley *et al.* \(1995\)](#) used the FENE-CR model to demonstrate the stabilizing role of finite extensibility in torsional flows and in the cone-and-plate configuration. While the finite-extensibility-induced stabilising argument can be made more precise ([Castillo Sánchez *et al.* 2022](#)) by accounting for shear thinning within the Pakdel-McKinley framework, rather surprisingly, we are not aware of the Dean-flow HSM being analysed quantitatively using any of the well-known nonlinear constitutive equations, such as the FENE-P/FENE-CR or Giesekus models. For this reason, and owing to the contrasting effect of finite extensibility on the HSM and CM demonstrated below, we revisit the HSM in viscoelastic Dean flow using both Oldroyd-B and FENE-P models. In doing so, we examine both axisymmetric and non-axisymmetric disturbances in the narrow-gap limit ($\epsilon \ll 1$), and for finite gap-width ratios ($\epsilon \sim O(1)$). The consideration of non-axisymmetric disturbances gains relevance because, while the HSM is present for axisymmetric disturbances, a non-zero azimuthal wavenumber can lead to a slight destabilization in certain cases, as has been shown by [Avgousti & Beris \(1993\)](#) for viscoelastic Taylor-Couette flow.

1.2. The centre-mode instability in viscoelastic shearing flows

In the narrow-gap limit ($\epsilon \rightarrow 0$), Wi has to increase as $\epsilon^{-1/2}$ in order for the hoop stress to remain in the leading order momentum balance. Thus, the HSM instability disappears, for a fixed Wi , as $\epsilon \rightarrow 0$, with the Dean flow configuration approaching plane Poiseuille flow. As mentioned above, the latter flow of an Oldroyd-B fluid was shown, by [Khalid *et al.* \(2021b\)](#), to be susceptible to the CM instability in the highly elastic ultra-dilute limit. The authors showed that the unstable mode has a phase speed close to the base-state maximum at the channel centreline (thence, the ‘centre mode’ terminology), with the critical Wi being $O(10^3)$. Furthermore, the most unstable mode is two-dimensional with no spanwise variation, owing to the existence of a Squire’s theorem for rectilinear shearing flows of an Oldroyd-B fluid ([Bistagnino *et al.* 2007](#)), which stipulates that two-dimensional disturbances are more unstable than three-dimensional ones. However, at such high Wi ’s, one expects shear thinning to become important ([Khalid *et al.* 2025](#)), potentially rendering the Oldroyd-B predictions less accurate. It is then appropriate to use, for instance, the FENE-P model which accounts for shear thinning of both the viscosity and first normal stress coefficient.

Rather surprisingly, and contrary to the aforementioned expectation of a stabilising influence of finite extensibility, [Buza *et al.* \(2022b\)](#) used the FENE-P model to show that the critical Wi decreased to $O(100)$. [Khalid *et al.* \(2025\)](#) have recently built on this finding, and presented a more comprehensive picture of the parameter regimes in which the elastic CM instability is present in channel flow of a FENE-P fluid. The authors showed that, while finite extensibility has the expected stabilising influence at lower elasticity numbers, it has a destabilising influence at higher E ’s, for $L \sim O(100)$. Such L ’s correspond to polyacrylamide solutions with molecular weights of $O(10^5)$, used in earlier experimental studies ([Choueiri *et al.* 2021](#)). As indicated above, the most unstable CM in plane Poiseuille flow has a non-zero streamwise wavenumber and zero spanwise wavenumber, which translates, in the Dean flow context, to two-dimensional perturbations varying in the azimuthal direction with no axial variations. In other words, contrary to the HSM above, the CM instability can arise even in the two-dimensional limit with axially invariant perturbations. Nevertheless, the absence of Squire’s theorem for any non-zero ϵ motivates us to also consider three-dimensional perturbations to arrive at the critical Wi as a function of ϵ . We note that, in light of [Yadav *et al.* \(2024\)](#)’s demonstration, of the existence of the CM instability for members of the Couette-Poiseuille family with non-monotonic velocity profiles, the present Dean-flow results should be relevant to the Taylor-Dean configuration as well, and thence, amenable to experiments ([Joo & Shaqfeh 1994](#)).

The rest of this paper is organized as follows. The governing equations for both Oldroyd-B and FENE-P models are discussed in Sec. 2.1. The base state velocity and stresses are discussed in Sec. 2.2 for the Oldroyd-B model, and in Sec. 2.3 for the FENE-P model. The linearization procedure is briefly introduced in Sec. 2.4, with Appendices A and B providing the full system of linearized equations governing small amplitude disturbances in the respective cases. Since earlier efforts examining the Dean flow configuration have solely focused on the unstable modes, we begin here by discussing the nature of the complete elastic eigenspectrum for Dean flow of both Oldroyd-B and FENE-P fluids in Sec. 3, with additional details of representative eigenspectra provided in Appendix C; sections 3.1 and 3.2 discuss the eigenspectra for the axisymmetric and non-axisymmetric cases, respectively. We then discuss the CM instability in viscoelastic Dean flow in Sec. 4. Herein, we first use the Oldroyd-B model in Sec. 4.1 to map out the unstable parameter regimes for arbitrary ϵ , both for two- and three-dimensional perturbations, and then proceed to examine the role of finite extensibility (using the FENE-P model) in Sec. 4.2. Section 5 begins with a brief recap of the

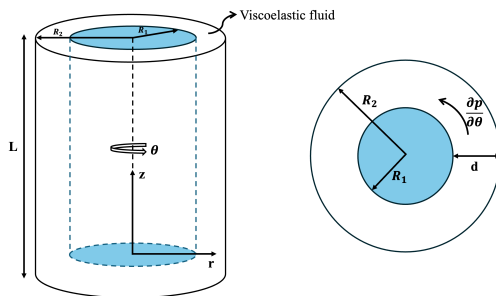


Figure 1: Schematic of the geometry and the coordinate system considered.

key results for HSM within the Oldroyd-B framework, following which we examine the role of finite extensibility on the HSM for both axisymmetric (Sec. 5.1) and non-axisymmetric (Sec. 5.2) disturbances. Appendix D provides a brief compilation of eigenfunctions of the relevant unstable modes. Finally, Sec. 6 provides a brief summary of the salient conclusions emerging from this effort, along with a discussion on which of the two modes (CM or HSM) is more critical in the viscoelastic parameter space.

2. Problem Formulation and numerical method

2.1. Governing Equations

We consider steady, fully developed pressure-driven flow of a viscoelastic fluid between concentric cylindrical surfaces with radii R_1 and R_2 ($R_1 < R_2$), corresponding to a gap width $d = R_2 - R_1$; the gap-width ratio being defined as $\epsilon = d/R_1$. A cylindrical coordinate system with r, θ, z denoting the radial, azimuthal and axial coordinates, respectively, shown in Fig. 1, is used with the pressure gradient imposed along the azimuth. The scales used for rendering dimensionless the physical quantities, associated with both Oldroyd-B and FENE-P models, are summarized in Table 1. The dimensionless continuity and inertialess Cauchy momentum equations take the form

$$\nabla \cdot \mathbf{v} = 0, \quad (2.1)$$

$$0 = -\nabla p + \beta \nabla^2 \mathbf{v} + (1 - \beta) \nabla \cdot \boldsymbol{\tau}, \quad (2.2)$$

with \mathbf{v} and p being the velocity and pressure fields, and $\boldsymbol{\tau}$ the polymeric stress tensor. In Eq. 2.2, $\beta = \eta_s/\eta$ is the solvent to solution viscosity ratio, where $\eta = \eta_s + \eta_p$ is the total (zero-shear) solution viscosity with η_p and η_s being the zero-shear polymer and solvent viscosities, respectively.

In the Oldroyd-B model (Larson 1988), the polymer solution is modelled as a non-interacting suspension of Hookean dumbbells, and the polymeric stress $\boldsymbol{\tau}$ is governed by:

$$\boldsymbol{\tau} + Wi \left(\frac{\partial \boldsymbol{\tau}}{\partial t} + \mathbf{v} \cdot \nabla \boldsymbol{\tau} - \nabla \mathbf{v}^\top \cdot \boldsymbol{\tau} - \boldsymbol{\tau} \cdot \nabla \mathbf{v} \right) = \left(\nabla \mathbf{v} + \nabla \mathbf{v}^\top \right). \quad (2.3)$$

Here, $Wi = \lambda U_m/d$ is the Weissenberg number. In the FENE-P model, the dumbbells are

Parameter	Dimensional Variable	Scale	Dimensionless variable
Length	r^*	d (gap width)	r
Velocity	\mathbf{v}^*	U_m (average velocity)	\mathbf{v}
Time	t^*	$\frac{d}{U_m}$	t
Pressure	p^*	$\frac{\eta U_m}{d}$	p
Polymeric stress	$\boldsymbol{\tau}^*$	$\frac{\eta_p U_m}{d}$	$\boldsymbol{\tau}$
Disturbance frequency	ω^*	λ (relaxation time)	ω
Conformation tensor	\mathbf{C}^*	$k_B T / H_{sp}$	\mathbf{C}

Table 1: Non-dimensionalisation scheme adopted in this study. Most symbols are defined in the text. Here, H_{sp} is the equilibrium spring constant in the Oldroyd-B and FENE-P models, k_B is the Boltzmann constant and T is the absolute temperature.

finitely extensible, and the polymeric contribution to the stress tensor is given by

$$\boldsymbol{\tau} = \frac{f\mathbf{C} - \mathbf{I}}{Wi}. \quad (2.4)$$

Here, \mathbf{C} denotes the dimensionless conformation tensor, while \mathbf{I} is the identity tensor representing the isotropic distribution of dumbbell conformations in the absence of an imposed flow. The Peterlin closure function f (Bird *et al.* 1980; Herrchen & Ottinger 1997) is defined as

$$f = \frac{L^2 - 3}{L^2 - \text{tr}(\mathbf{C})}, \quad (2.5)$$

where L represents the dimensionless extensibility parameter, defined as the ratio of the polymer's maximum extension to its equilibrium root-mean-square value; the Oldroyd-B model being attained in the limit of infinite extensibility viz., $L \rightarrow \infty$, when $f \rightarrow 1$. The conformation tensor is governed by the following evolution equation:

$$\frac{\partial \mathbf{C}}{\partial t} + \mathbf{v} \cdot \nabla \mathbf{C} - \nabla \mathbf{v}^\top \cdot \mathbf{C} - \mathbf{C} \cdot \nabla \mathbf{v} = -\boldsymbol{\tau}. \quad (2.6)$$

2.2. Base State for the Oldroyd-B Model

The base state velocity profile for Dean flow of an Oldroyd-B fluid is identical to its Newtonian counterpart (Diprima 1959; Joo & Shaqfeh 1992), and therefore, independent of Wi . The non-dimensional velocity profile, after using the coordinate transformation $r^* = R_1(1 + \epsilon y)$, is given by:

$$\bar{\mathbf{v}} = \begin{bmatrix} \bar{v}_r \\ \bar{v}_\theta \\ \bar{v}_z \end{bmatrix} = \begin{bmatrix} 0 \\ U(y) \\ 0 \end{bmatrix}, \quad (2.7)$$

$$U(y) = \frac{-K \left[(1 + \epsilon y) - \frac{1}{(1 + \epsilon y)} \right] + [(1 + \epsilon y) \ln(1 + \epsilon y)]}{K \left[\frac{\ln(1 + \epsilon)}{\epsilon} \right] - \frac{1}{4}(2 + \epsilon)}, \quad (2.8)$$

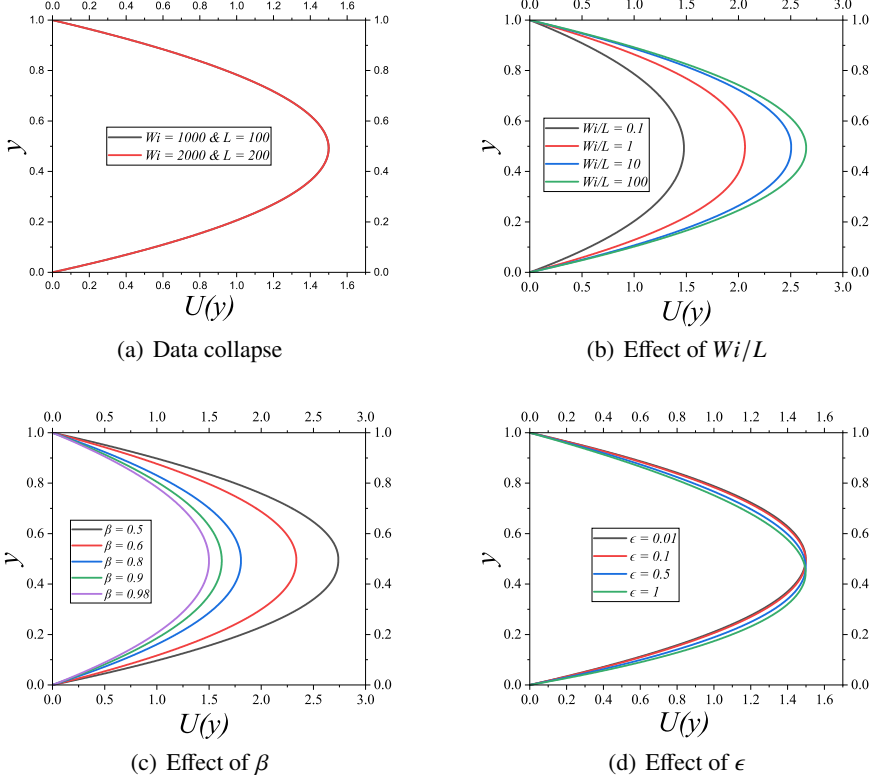


Figure 2: Dean flow velocity profiles for a FENE-P fluid: (a) $\beta = 0.98$ and $\epsilon = 0.1$ for two (Wi, L) pairs, with $Wi/L = 10$; (b) $\beta = 0.5$ and $\epsilon = 0.1$ with varying Wi/L ; (c) master curves for $Wi/L = 10$ and $\epsilon = 0.1$ for varying β ; (d) master curves for $Wi/L = 10$ and $\beta = 0.9$ for varying ϵ .

where $K = \frac{(1+\epsilon)^2 \ln(1+\epsilon)}{(1+\epsilon)^2 - 1}$, and the average velocity that has been used as the scale in Eq. 2.8, is given by: $U_m = \frac{\partial p}{\partial \theta} \frac{R_1}{2\eta} \left(K \left[\frac{\ln(1+\epsilon)}{\epsilon} \right] - \frac{1}{4}(2 + \epsilon) \right)$. The polymer contribution to the base state stress tensor is given by

$$\bar{\tau} = \begin{bmatrix} \bar{\tau}_{rr} & \bar{\tau}_{r\theta} & \bar{\tau}_{rz} \\ \bar{\tau}_{\theta r} & \bar{\tau}_{\theta\theta} & \bar{\tau}_{\theta z} \\ \bar{\tau}_{zr} & \bar{\tau}_{z\theta} & \bar{\tau}_{zz} \end{bmatrix} = \begin{bmatrix} 0 & U' - \frac{\epsilon}{1+\epsilon y} U & 0 \\ U' - \frac{\epsilon}{1+\epsilon y} U & 2Wi(U' - \frac{\epsilon}{1+\epsilon y} U)^2 & 0 \\ 0 & 0 & 0 \end{bmatrix}, \quad (2.9)$$

where $\zeta' \equiv D\zeta \equiv \frac{d\zeta}{dy}$.

2.3. Base State for the FENE-P model

The base state velocity field, conformation tensor, and the polymer stress tensor in this case are given by

$$\bar{\mathbf{v}} = \begin{bmatrix} \bar{v}_r \\ \bar{v}_\theta \\ \bar{v}_z \end{bmatrix} = \begin{bmatrix} 0 \\ U(y) \\ 0 \end{bmatrix}, \quad (2.10)$$

$$\bar{\mathbf{C}} = \begin{bmatrix} \bar{C}_{rr} & \bar{C}_{r\theta} & \bar{C}_{rz} \\ \bar{C}_{\theta r} & \bar{C}_{\theta\theta} & \bar{C}_{\theta z} \\ \bar{C}_{zr} & \bar{C}_{z\theta} & \bar{C}_{zz} \end{bmatrix} = \begin{bmatrix} \frac{1}{\bar{f}} & \frac{Wi \bar{C}_{rr}(U' - \frac{U\epsilon}{1+\epsilon y})}{\bar{f}} & 0 \\ \frac{Wi \bar{C}_{rr}(U' - \frac{U\epsilon}{1+\epsilon y})}{\bar{f}} & \frac{1+2Wi \bar{C}_{r\theta}(U' - \frac{U\epsilon}{1+\epsilon y})}{\bar{f}} & 0 \\ 0 & 0 & \frac{1}{\bar{f}} \end{bmatrix}, \quad (2.11)$$

$$\bar{\boldsymbol{\tau}} = \begin{bmatrix} \bar{\tau}_{rr} & \bar{\tau}_{r\theta} & \bar{\tau}_{rz} \\ \bar{\tau}_{\theta r} & \bar{\tau}_{\theta\theta} & \bar{\tau}_{\theta z} \\ \bar{\tau}_{zr} & \bar{\tau}_{z\theta} & \bar{\tau}_{zz} \end{bmatrix} = \begin{bmatrix} 0 & \bar{C}_{rr}(U' - \frac{U\epsilon}{1+\epsilon y}) & 0 \\ \bar{C}_{rr}(U' - \frac{U\epsilon}{1+\epsilon y}) & 2\bar{C}_{r\theta}(U' - \frac{U\epsilon}{1+\epsilon y}) & 0 \\ 0 & 0 & 0 \end{bmatrix}. \quad (2.12)$$

By combining Eq. 2.5 in the base state with $\bar{\tau}_{r\theta} = \bar{C}_{rr}(U' - \frac{U\epsilon}{1+\epsilon y}) = \frac{U' - \frac{U\epsilon}{1+\epsilon y}}{\bar{f}}$ and eliminating \bar{f} , we obtain

$$\tau_{r\theta}^3 + \frac{L^2}{2Wi^2}\tau_{r\theta} - \frac{L^2}{2Wi^2}\left(U' - \frac{U\epsilon}{1+\epsilon y}\right) = 0. \quad (2.13)$$

This equation for $\tau_{r\theta}$ is coupled to $U(y)$ through the θ -component of Eq. 2.2, which provides a second relation between $\tau_{r\theta}$ and $U(y)$. The two equations are simultaneously solved, numerically, to obtain the base state fields; more details regarding the numerical procedure can be found in [Tej et al. \(2024\)](#). The base state velocity profile does depend on Wi and L , although only via the combination Wi/L for $L \gg 1$. Figure 2(a) illustrates the collapse of the profiles for different (Wi, L) pairs, with Wi/L fixed (and for $L \gg 1$). This collapse, first demonstrated by [Yamani & McKinley \(2023\)](#) for simple shear flow, was later generalized by [Tej et al. \(2024\)](#) to steady unidirectional rectilinear and curvilinear shear flows of a FENE-P fluid. Figure 2(b) shows the velocity profiles for different Wi/L , for a fixed β , where the maximum velocity U_{max} is seen to increase with increasing Wi/L , due to shear thinning; when normalized by U_{max} , expectedly, the profiles would be flatter for larger Wi/L . The effect of changing β at a fixed Wi/L and ϵ is shown in Fig. 2(c), where shear thinning again leads to an increased maximum, relative to the Oldroyd-B limit, for the smaller β values; the profile reverts to the Newtonian form for $\beta \rightarrow 1$. Finally, the role of varying ϵ is shown in Fig. 2(d) where, for $\epsilon \ll 1$ (narrow-gap limit), the maximum velocity occurs at the centreline; this location shifting towards the inner cylinder for finite gap-width ratios.

2.4. Linear stability analysis

A temporal linear stability analysis is carried out wherein the aforementioned base states (Eqs. 2.7-2.9 for the Oldroyd-B model and Eqs. 2.10-2.12 for the FENE-P model) are subjected to small-amplitude perturbations. We consider both axisymmetric and non-axisymmetric disturbances in this study. The total velocity, pressure and stress are each

Dean Flow	α_c	$\epsilon^{1/2}Wi_c$
Joo and Shaqfeh	6.6 ± 0.1	4.06 ± 0.02
Present	6.56	4.06

Table 2: Validation of UCM ($\beta = 0$) results with those of Joo & Shaqfeh (1992).

expressed as a sum of a base-state contribution ($\bar{\chi}$) and an imposed perturbation ($\hat{\chi}$):

$$\chi = \bar{\chi} + \hat{\chi}, \quad (2.14)$$

where the variable χ represents any of the field variables. Next, the perturbation fields are assumed to be of the Fourier mode form:

$$\hat{\chi}(y, z, \theta, t) = \tilde{\chi}(y) \exp \left[i \left(\alpha z + n\theta - \frac{\omega}{Wi} t \right) \right]. \quad (2.15)$$

Here α and n are the axial and azimuthal wavenumbers respectively and $\omega = \omega_r + i\omega_i$ is the complex frequency. Note that axisymmetric disturbances correspond to $n = 0$, while $\alpha = 0$ corresponds to two-dimensional perturbations in the r - θ plane; three-dimensional disturbances correspond to $\alpha \neq 0$ and $n \neq 0$. The flow is temporally unstable if $\omega_i > 0$. Substituting Eq. 2.15 in the linearized versions of (2.1), (2.2) and (2.3) we obtain the set of governing equations, given in Appendices A and B for the Oldroyd-B and FENE-P models, respectively.

2.5. Numerical methods

We solved the linearized governing equations using a spectral method (Trefethen 2000; Weideman & Reddy 2000) and a shooting procedure. In the spectral method, we expand the dynamical variables as a finite sum of Chebyshev polynomials, and substitute this expansion in the linearized governing equations – (A 1) – (A 10), for the Oldroyd-B model or (B 1) – (B 4) for the FENE-P model – to obtain a generalized eigenvalue problem as follows

$$\mathbf{A}\mathbf{x} = \omega\mathbf{B}\mathbf{x}. \quad (2.16)$$

Here \mathbf{A} and \mathbf{B} are coefficient matrices, with $\mathbf{x} = (\tilde{v}_r, \tilde{v}_\theta, \tilde{v}_z, \tilde{p}, \tilde{\tau}_{rr}, \tilde{\tau}_{r\theta}, \tilde{\tau}_{rz}, \tilde{\tau}_{\theta\theta}, \tilde{\tau}_{\theta z}, \tilde{\tau}_{zz})^T$ for the Oldroyd-B model and $\mathbf{x} = (\tilde{v}_r, \tilde{v}_\theta, \tilde{v}_z, \tilde{p}, \tilde{C}_{rr}, \tilde{C}_{r\theta}, \tilde{C}_{rz}, \tilde{C}_{\theta\theta}, \tilde{C}_{\theta z}, \tilde{C}_{zz})^T$ for the FENE-P model. The size of the \mathbf{A} matrix is $10N \times 10N$, where N is the number of Gauss–Lobatto collocation points. The generalized eigenvalue problem is solved using the ‘eig’ solver of *Matlab*. Depending on the parameter regime, the number of collocation points N required to capture physically genuine eigenvalues differs. Convergence in this method is achieved by comparing the eigenspectra for two different values of N , and filtering them using a prescribed tolerance. The shooting method is based on a Runge-Kutta integrator with a Gram-Schmidt orthonormalization procedure (Ho & Denn 1977), and a Newton-Raphson iteration for the eigenvalue. This procedure is implemented only for the Oldroyd-B model. It is known that spectral method can give unphysical (spurious) eigenvalues (Schmid & Henningson 2001), but the shooting method gives genuine eigenvalues, given a good initial guess. Thus, the genuineness of the eigenvalues, obtained from the spectral method, is confirmed by providing them as initial guesses for the shooting method. To benchmark the implementation of our numerical methodology in the narrow-gap limit, we compare (Table 2 and Figure 3) results from our procedure with those of Joo & Shaqfeh (1992), finding excellent agreement.

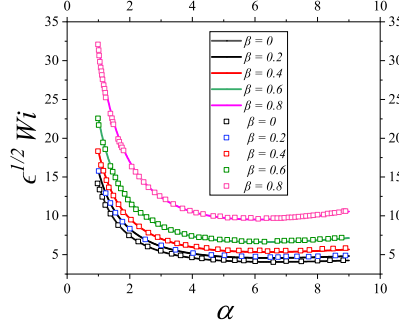


Figure 3: Benchmarking of neutral curves obtained from our numerical (spectral-cum-shooting) procedure (for $Re = 0$, $n = 0$) with those of Joo & Shaqfeh (1992), for Dean flow of an Oldroyd-B fluid, for different β . Continuous lines show results from the present work, while discrete points represent the data of Joo & Shaqfeh (1992).

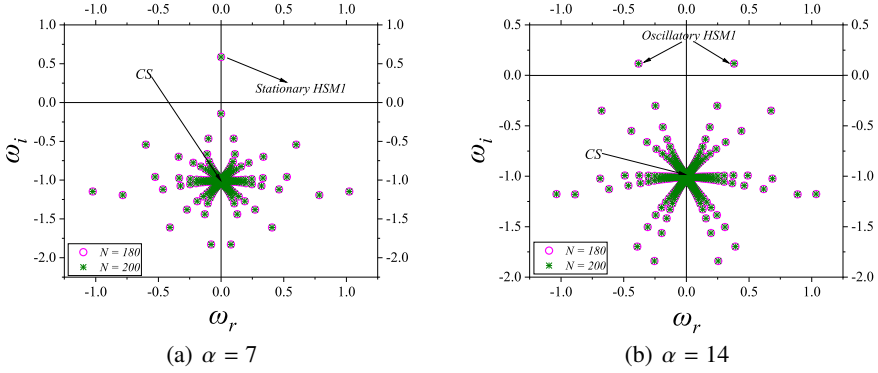


Figure 4: Eigenspectrum showing stationary ($\alpha = 7$) and propagating ($\alpha = 14$) modes of instability via the HSM1 mode in Dean flow of an Oldroyd-B fluid at $Re = 0$, $n = 0$, $\beta = 0.98$, $\epsilon = 0.1$, and $Wi = 25$.

3. Nature of the elastic spectrum in Dean flow

Herein, we provide an overview of the elastic eigenspectrum for Dean flow, before proceeding to discuss the two classes of unstable modes (viz., CM and HSM) in subsequent sections. A clear understanding of the structure of the elastic spectrum is necessary to interpret the origin of different unstable modes, and to also enable us to distinguish them from one another.

3.1. Axisymmetric disturbances ($n = 0$)

Figure 4 shows the axisymmetric elastic spectrum for Dean flow of an Oldroyd-B fluid at two different axial wavenumbers (α). For both α 's, there appear to be a large number of discrete modes, perhaps even an infinite number of them, accumulating towards the point ($\omega_r = 0$, $\omega_i = -1$); this point is shown below to be part of the continuous spectrum for $n = 0$. In both spectra, there are also unstable modes, which could either be stationary ($\omega_r = 0$; see Fig. 4(a)) or propagating ($\omega_r \neq 0$; see Fig. 4(b)) ones; in the latter case they appear symmetrically on either side of the imaginary axis. For the stationary scenario, the least stable/most unstable of the discrete modes is the classical axisymmetric HSM, originally identified by Joo & Shaqfeh (1991, 1994), and is labelled as ‘HSM1’ henceforth. A more

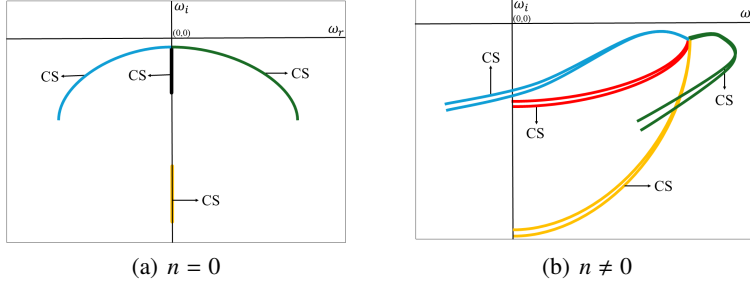


Figure 5: Schematic of the continuous spectra branches in Dean flow of a FENE-P fluid with $Wi/L \sim O(1)$ and $\beta \rightarrow 1$.

detailed discussion of the parameter regimes in which HSM1 is stationary or propagating is provided in Appendix C. It will be seen therein that the stationary-to-propagating modal transition can happen with an increase in α for a fixed Wi , or for a fixed α and with decreasing Wi .

Now, it is well known that the eigenspectra for viscoelastic flows also contain (stable) continuous spectra (CS) of eigenvalues (Wilson *et al.* 1999; Roy *et al.* 2022). These are obtained by setting the coefficient of the highest order derivative of the governing linearized equation for the wall-normal velocity perturbation to zero. For rectilinear flows such as plane Couette and Poiseuille flows of an Oldroyd-B fluid, this leads to two distinct CS with decay rates $\omega_i = -1$ and $\omega_i = -1/\beta$. In general, these CS are horizontal line segments in the ω_r - ω_i plane whose length is proportional to $k\Delta V$, with ΔV being the base range of velocities, and k the streamwise wavenumber. Along similar lines, for Dean flow, the horizontal extent of the CS is proportional to $n\Delta V$. For Dean flow subjected to axisymmetric disturbances ($n = 0$) as in Fig. 4, the CS, within the Oldroyd-B framework, therefore degenerate to a pair of points on the imaginary axis with $\omega_i = -1$ and $-1/\beta$; the two points approaching each other in the limit $\beta \rightarrow 1$ ($\beta = 0.98$ in Fig. 4).

We now turn to the effect of L on the spectra. As L is decreased, owing to shear thinning of rheological properties, the nature of CS for both rectilinear and curvilinear shearing flows, including Dean flow in particular, is significantly more complex compared to that for the Oldroyd-B fluid mentioned above. In the interests of brevity, we provide here only the key features of the CS that are relevant to the present work; a detailed discussion is provided in Mohanty *et al.* (2025). A schematic of the CS for Dean flow, pertinent to the dilute-solution limit ($\beta \gtrsim 0.95$), and for $Wi/L \sim O(1)$ (so shear thinning effects remain significant), is shown in Fig. 5(a) for $n = 0$. As L is decreased from the Oldroyd-B limit, the ‘point CS’ on the imaginary axis, in the Oldroyd-B limit mentioned above, turn into vertical line segments. The two line segments are shown to be distinct in the schematic, but may overlap depending on the particular choice of parameters. The reason underlying the extended CS, even for $n = 0$, is due to the variation of the base-state Peterlin function \bar{f} as a function of the wall-normal coordinate, which leads to a range of relaxation times, and thence, decay rates. Concurrently, a pair of symmetrically placed ‘wing’-like CS emerge on either side of the imaginary axis (Mohanty *et al.* 2025). As L is decreased, the horizontal extent of the wings and the vertical line segments (belonging to the CS) increases. The computed numerical spectra illustrating these features are shown in Fig. 6, for different L ’s, at a fixed Wi .

Apart from the CS, the spectra in Fig. 6 also contain discrete modes, which are not depicted in the Fig. 5(a) schematic. In fact, Figs. 6(a)–6(h) show that decreasing L has a strong influence on the configuration of discrete modes. In contrast to the Oldroyd-B case above, where

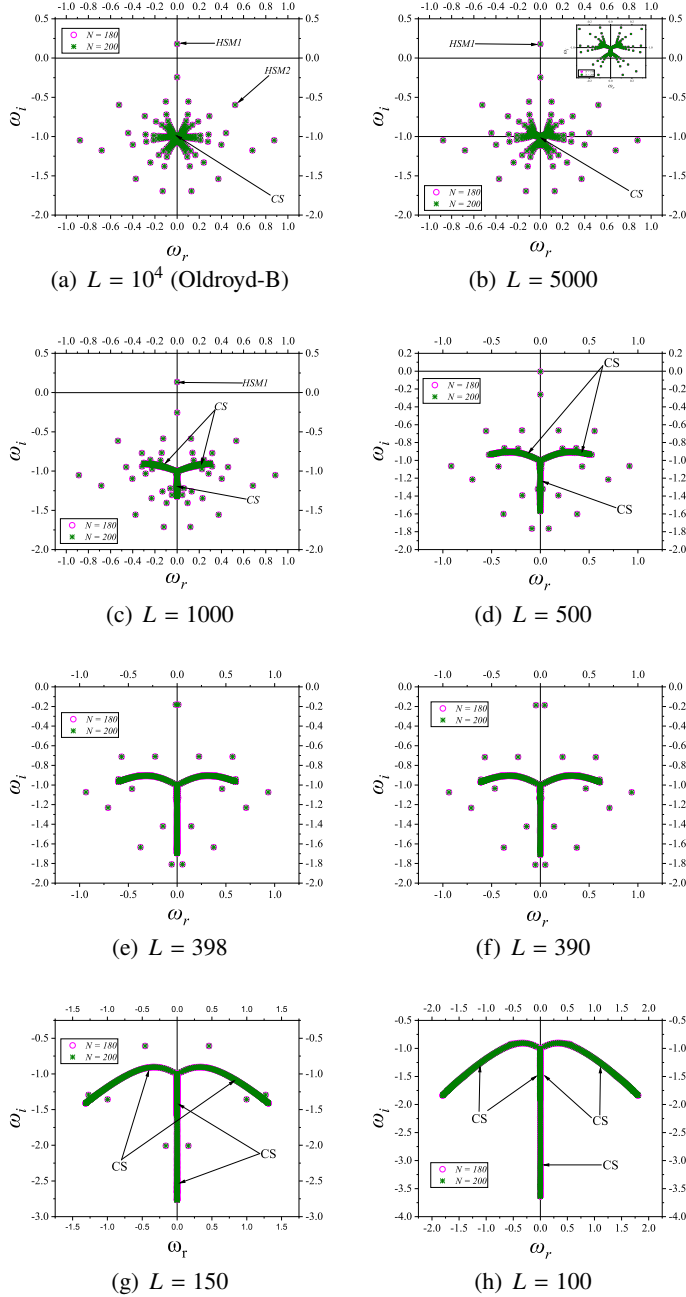


Figure 6: Eigenspectra for Dean flow of FENE-P fluids at different L 's; data for $n = 0$, $\epsilon = 0.1$, $\alpha = 7$, $\beta = 0.98$, $Wi = 20$, and $Re = 0$.

there were (apparently) an infinite number of discrete modes accumulating at the (point) CS, a decrease in L leads to a progressive reduction in the number of modes. When L is decreased to 398, the most unstable mode changes from a stationary one, to a pair of propagating ones; this change is due to a coalescence of HSM1 and the next (least stable) mode, followed by a

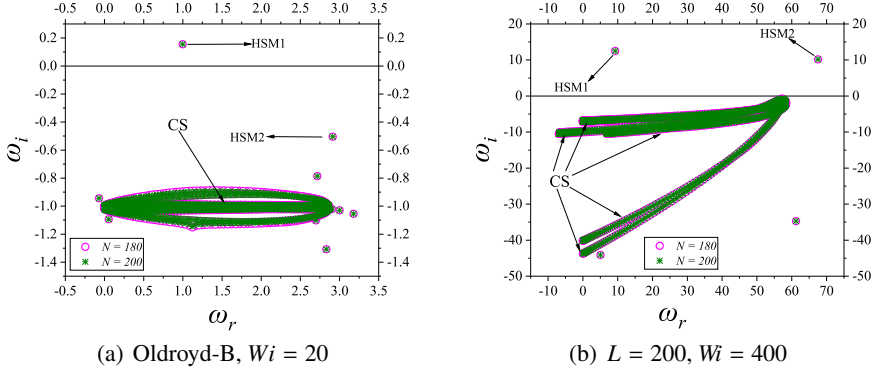


Figure 7: Eigenspectrum for non-axisymmetric ($n = 1$) disturbances showing both HSM1 and HSM2 in Dean flow of an Oldroyd-B and FENE-P ($L = 200$) fluids. Data for $\alpha = 7$, $\beta = 0.98$, and $\epsilon = 0.1$.

bifurcation. The propagating pair moves down towards the CS as L is decreased further, this shear-thinning-induced stabilization being discussed further in Sec. 5.1 below. Eventually, for $L = 100$, there are no discrete modes, either stable or unstable, and the spectrum comprises solely of modes belonging to the CS for $Wi \gtrsim 16$ (see Fig. 6(h)).

3.2. Non-axisymmetric disturbances ($n \neq 0$)

The schematic of the CS for $n \neq 0$ is shown in Fig. 5(b) for FENE-P fluids with $Wi/L \sim O(1)$; again, the details of how these are obtained theoretically are discussed in Mohanty *et al.* (2025). There are four distinct CS (for $L \gtrsim 50$) in Fig. 5(b), and each CS has two branches. These branches arise due to the lack of a mid-plane symmetry in Dean flow, and degenerate in the case of plane-Poiseuille flow. The actual numerical spectra for a nonzero n ($n = 1$), for both the Oldroyd-B and FENE-P cases, are shown in Figs. 7(a) and 7(b).

In Fig. 7(a), we present the spectra for the same set of parameters as for the axisymmetric case ($n = 0$) in Fig. 6(a). For $n = 1$, the theoretical CS are no longer points even in the Oldroyd-B fluid, but are horizontal line segments located again at $\omega_i = -1$ and $-1/\beta$; these are only resolved as balloons in Fig. 7(a).

The constitution of the discrete modes in the spectra for $n = 1$ also differs qualitatively from those for $n = 0$. In particular, the discrete modes in Fig. 6(a) (for $n = 0$) with negative ω_r are virtually absent in the spectrum for $n = 1$ (see Fig. 7(a)). The absence is understandable since a negative ω_i implies a propagation in the direction opposite to the base state shear flow, which is an unlikely possibility in the absence of inertia. We have verified (data not shown) that as n is increased continuously from 0 to 1, there is also an overall reduction in the number of discrete modes, this reduction arising because many of these discrete modes disappear into the CS. In Fig. 7(a), the classical hoop stress mode (HSM1) is the mode that dictates the instability in the Oldroyd-B limit. This mode could be stationary or propagating for axisymmetric disturbances, but is propagating for non-axisymmetric disturbances.

Amidst the collection of other discrete modes, we also identify another mode (labelled ‘HSM2’), which remains stable at the Wi chosen in Fig. 7(a). One reason behind singling out HSM2, amongst other discrete modes, maybe seen in Fig. 7(b), where it is unstable with a growth rate that is nearly equal to that of HSM1, for $L = 200$, albeit at a higher $Wi = 400$. Figures 8(a)–8(d) show the complete spectra for the Oldroyd-B fluid at different Wi , with both HSM1 and HSM2 identified, while Fig. 9 tracks the loci of HSM1 and HSM2 in the complex-

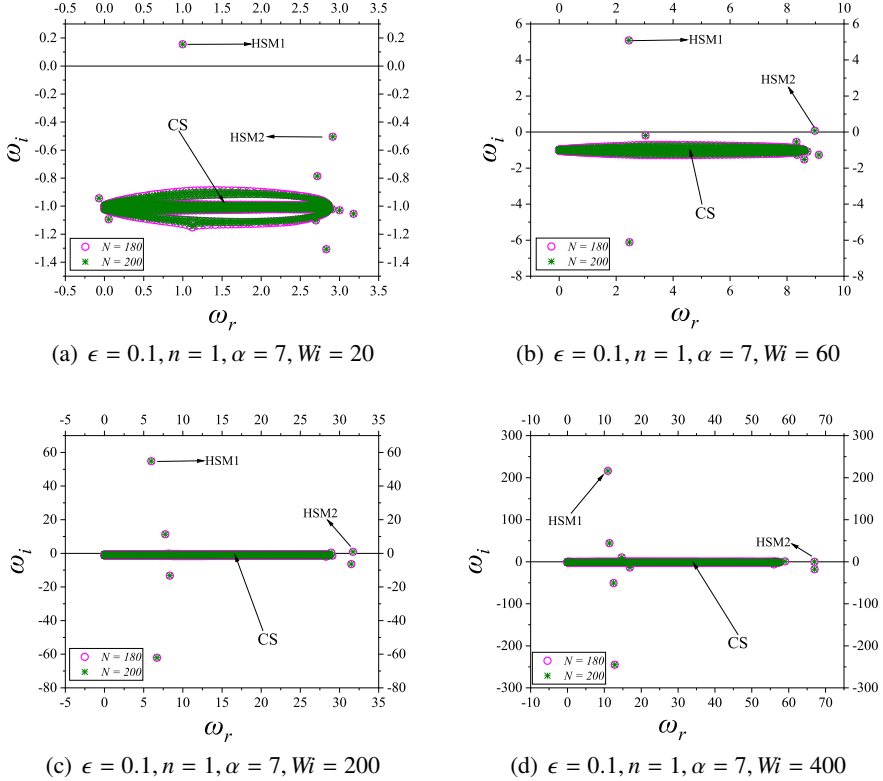


Figure 8: Eigenspectra showing HSM1 and HSM2 in Dean flow of an Oldroyd-B fluid at $Re = 0, \alpha = 7, \beta = 0.98, \epsilon = 0.1, n = 1$ for different Wi 's.

ω plane with increasing Wi . The inset in this figure shows the variation of the growth rate with Wi for both modes. While an increase in Wi has a monotonic destabilizing influence on HSM1, it has a non-monotonic effect on HSM2, with this mode being unstable only over an intermediate range of Wi , and eventually stabilizing at sufficiently high Wi ; note that the growth rates of HSM2 are much smaller compared to those of HSM1.

Returning to Fig. 7(b), the spectrum (for $L = 200$) also demonstrates the presence of multiple non-trivial CS branches, for $n \neq 0$, which nevertheless conform to the schematic shown in Fig. 5(b) above. While Fig. 7(b) is for $L = 200$, HSM2 is further destabilized with decreasing L , leading to it becoming the critical mode for sufficiently small L , in certain regions of the parameter space. This is in contrast to the Oldroyd-B limit, where HSM1 is always the critical mode. The detailed behaviour of HSM1 and 2 growth rates, for the FENE-P case, is discussed in Sec. 5.2. It is nevertheless worth a brief mention here, since the unexpected destabilizing effect of finite elasticity first seen for the CM by [Buza et al. \(2022b\)](#), is also present for HSM2.

We end our discussion of the elastic spectrum with Fig. 10, which presents the elastic spectrum for $\beta = 0.994$ and $\epsilon = 0.1$; the spectrum includes an unstable CM. The contrast in the choice of parameters, relative to the spectra in Figs. 4 and 6 above, is on account of the restricted nature of the unstable portion of the parameter space, in the limit of $\epsilon \rightarrow 0$, corresponding to plane Poiseuille flow – the centre-mode instability only exists for $\beta > 0.99052$ in this limit, and for $Wi \sim O(300)$ (within the Oldroyd-B model; see [Khalid et al.](#)

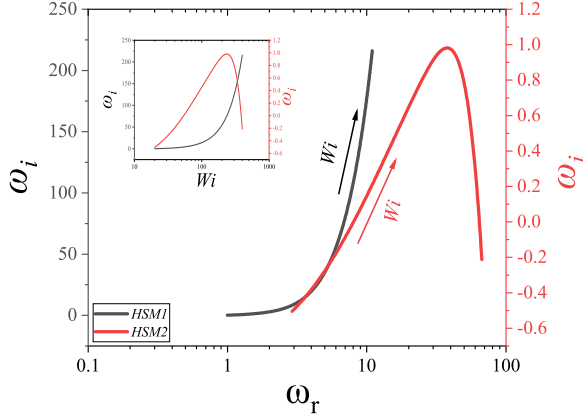


Figure 9: Variation of HSM1 and HSM2 growth rates with increasing Wi . Note the difference in scales of the left and right y-axes (for HSM1 and HSM2, respectively) on account of the vast difference in the growth rate magnitudes. The arrows indicate the direction of increasing Wi . The inset shows the variation of ω_i with Wi for both the modes. Data for $Re = 0$, $\alpha = 7$, $\beta = 0.98$, $\epsilon = 0.1$, $n = 1$.

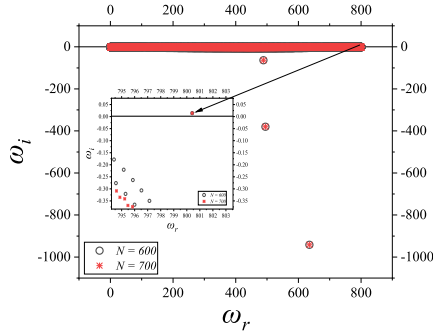


Figure 10: Eigenspectrum showing the presence of the centre mode in Dean flow of an Oldroyd-B fluid (with $n = 16$, $\epsilon = 0.1$, $\alpha = 0$, $\beta = 0.994$ and $Wi = 350$). The inset shows zoomed-in view highlighting the region near the unstable centre mode; the discrete eigenvalues obtained for $N = 600$ and $N = 700$ show good convergence.

2021b). It is pertinent to note here that the Weissenberg number used in the present study and the one used in the earlier effort of [Khalid et al. \(2021b\)](#) are related by a factor of three, as we elaborate in Sec. 4.1 below. The role of decreasing L on the CM is discussed subsequently in Sec. 4.2.

4. Elastic centre-mode instability in Dean flow

Having described the overall structure of the spectrum in the regions of parameter space relevant to the two elastic instabilities, we first focus on the results for the CM instability, using the Oldroyd-B model, both in the narrow- and finite-gap regimes. We then proceed to explore the role of finite extensibility. Owing to the difficulty in the experimental realization of pure Dean flow, the existing observations (by [Joo & Shaqfeh 1994](#)) are for a subset of the Taylor-Dean family with zero azimuthal flow rate. As noted in the Introduction, the latter was

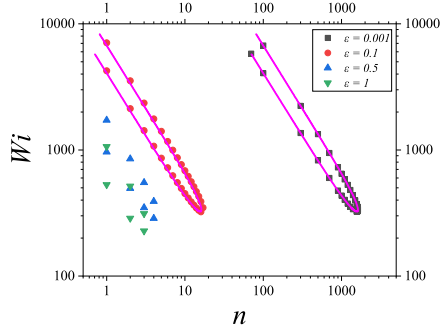


Figure 11: The centre-mode instability in Dean flow of an Oldroyd-B fluid at $Re = 0$, with $\alpha = 0$: Neutral curves in the Wi - n plane at different ϵ 's for $\beta = 0.994$. For $\epsilon = 0.001$ and 0.1 , we also plot the neutral curve (continuous lines) obtained for pressure-driven flow in a rectilinear channel (Khalid *et al.* 2021b); incipient departure from the $n \sim \epsilon^{-1}$ scaling is evident in the comparison for $\epsilon = 0.1$.

realised in the gap between concentric cylinders, with the flow driven by rotation of either cylinder, and with the (adverse) pressure gradient arising from a vertical obstruction in the gap at a particular azimuthal location. For this setup, the unidirectional approximation of the base Taylor-Dean velocity profile is strictly valid only for $\epsilon \ll 1$, when ‘end effects’ due to the azimuthal obstruction are negligible. For $\epsilon \sim O(1)$, the gap width is comparable to the radius of the inner cylinder, and the unidirectional velocity profile given by Eq. 2.8 will no longer be representative of the actual flow (which deviates from uni-directionality in a region whose size becomes comparable to R_1). Therefore, keeping in mind relevance to experiments, we restrict our results below to $\epsilon \leq 1$.

4.1. Centre-mode instability within the Oldroyd-B framework

In the narrow-gap limit, $\epsilon \ll 1$, the base state Dean profile approaches plane Poiseuille flow, and we therefore begin with a validation of our numerical procedure by recovering the expected results (Khalid *et al.* 2021b) in the aforementioned limit. To establish the connection between the two flows, note that the angular displacement θ in the Dean (cylindrical) geometry is the ratio of the arc length x^* to the radial distance r^* , that is, $\theta = \frac{x^*}{r^*}$. In the narrow-gap limit, $r^* = R_1(1 + \epsilon y) \approx R_1$, and the above relation reduces to $\theta = x^*/R_1$, leading to $n\theta = nx^*/R_1$. Thus, n/R_1 in cylindrical coordinates, for Dean flow, corresponds to the dimensional streamwise wavenumber k^* for plane Poiseuille flow; using $k^* = 2k/d$ gives $n = 2k/\epsilon$. Now, Khalid *et al.* (2021b) report the minimum critical Weissenberg number ($Wi_c = 973.8$) and critical wavenumber ($k_c = 0.783$), for $\beta = 0.994$, for the elastic CM in plane Poiseuille flow, and these values arise from the authors using the maximum speed (U_{max}) and the half gap-width ($d/2$) as the characteristic velocity and length scales; the Weissenberg number and non-dimensional wavenumber being defined as $Wi_K = \frac{\lambda U_{max}}{(d/2)}$ and $k = k^*d/2$ respectively. In the present study, the Weissenberg number is defined as $Wi = \lambda U_m/d$. Noting that the ratio of maximum to mean speed is $3/2$ for plane Poiseuille flow, yields the following relation between the critical parameters: $Wi/Wi_K = 1/3$, $n_c = 2k_c/\epsilon$, in turn leading to $Wi_c = 324.6$ and $n_c = 1566$ in the narrow-gap limit. Figure 11 shows the neutral curves in the Wi - n plane for ϵ 's ranging from 0.001 to 1 . The figure also shows the neutral curves obtained by Khalid *et al.* (2021b) for pressure-driven (rectilinear) channel flow, highlighting the excellent agreement (for $\epsilon = 0.001$) between the Dean and channel flow cases. Although it was found convenient to vary n continuously, when tracking

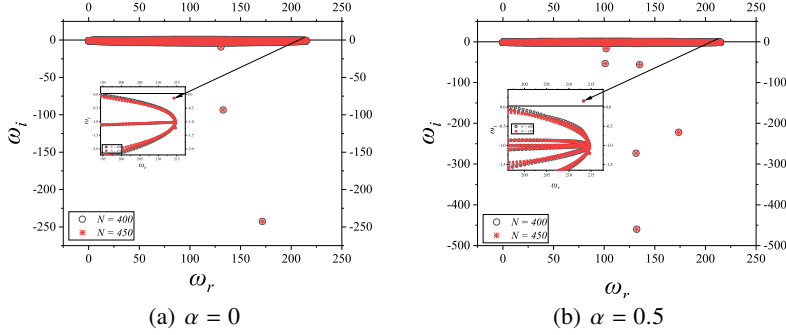


Figure 12: Eigenspectra showing the destabilising role of axially varying perturbations on the centre mode in Dean flow of an Oldroyd-B fluid. Data for $n = 1$, $\epsilon = 0.1$, $\beta = 0.98$ and $Wi = 1500$. The insets show the enlarged region of the spectra near the centre mode.

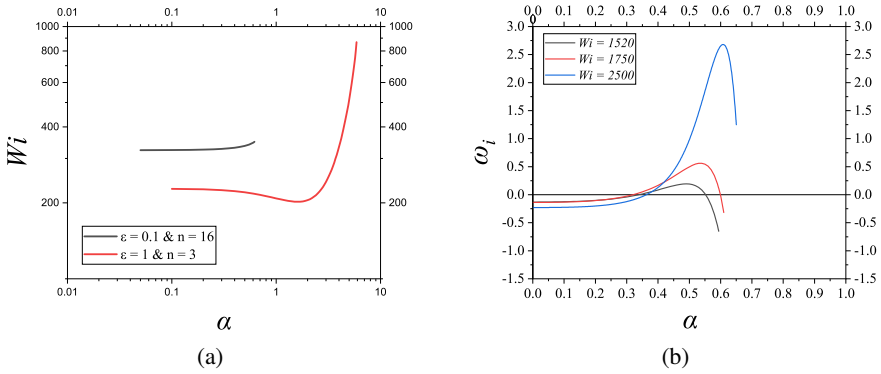


Figure 13: (a) Neutral curves in the Wi - α plane for two (ϵ, n) pairs for $\beta = 0.994$. (b) Variation of ω_i with α showing the destabilisation of the centre mode in Dean flow for non-zero α . Data for the Oldroyd-B fluid with $n = 1$, $\epsilon = 0.1$ and $\beta = 0.98$.

the neutral points in the Wi - n plane using the shooting procedure, it is worth keeping in mind that the discreteness of n implies that the critical Wi corresponds to the integer n closest to the minimum of the tongues in Fig. 11. There is a leftward movement of the neutral curves with increasing ϵ , as is expected on account of the $n \sim \epsilon^{-1}$ scaling for $\epsilon \ll 1$; although, this movement slows down for finite ϵ . There is, in addition, an overall lowering of the unstable tongue, resulting in a decrease in the critical Weissenberg number Wi_c with an increase in ϵ .

Next, Fig. 12 examines the role of axial variation ($\alpha \neq 0$) of perturbations. In Fig. 12(a), for the chosen parameter values, the CM is stable for two-dimensional disturbances (i.e., $n \neq 0$ and $\alpha = 0$). However, when three-dimensional disturbances are introduced (i.e., both $n \neq 0$ and $\alpha \neq 0$), surprisingly, the CM becomes unstable (Fig. 12(b)). That is to say, the introduction of an axial variation destabilizes the centre mode. A further increase in α was found to lead to eventual stabilization, however. This implies that, in order to obtain the critical Wi , it is in principle necessary to minimize over both n and α . To this end, in Fig. 13(a), we show the neutral curves in the Wi - α plane for a fixed n , with the latter taken to be the critical value for $\alpha \rightarrow 0$. The monotonic increase in Wi_c with increasing α , for $\epsilon = 0.1$, appears to be consistent with existence of a Squire's theorem in the limit of $\epsilon \rightarrow 0$ (that is, for rectilinear shearing flows; see Bistagnino *et al.* 2007). That this is not the case is shown in

ϵ	n_c	Wi_c
0.001	1566	324.61
0.1	16	323.38
1	3	227.76

Table 3: Variation of critical Weissenberg number (Wi_c) with ϵ at $\beta = 0.994$ and $Re = 0$ for the centre mode in Dean flow of an Oldroyd-B fluid.

Fig. 13(b), where we plot the variation of growth rate as a function of α , for Wi significantly larger than the threshold for neutral stability, but for a $\beta (= 0.98)$ that lies below the rectilinear channel-flow threshold for the chosen ϵ . Even for the relatively low value, $\epsilon = 0.1$, an increase in α is seen to lead to an unstable CM, where no such instability existed for $\alpha = 0$. The initial increase in growth rate, however, is followed by stabilization for sufficient large α . Returning to Fig. 13(a), for $\epsilon = 1$, the Wi - α neutral curve shows that, while there is an initial destabilization (a decrease in Wi up until $\alpha \approx 2$, in contrast to $\epsilon = 0.1$), this is followed by a stabilizing effect at sufficiently large α . On the whole, both the growth rates and the critical Wi exhibit a non-monotonic dependence on α . Thus, there exist three-dimensional perturbations that are more unstable than two-dimensional ones, in apparent contradiction with Squire's theorem for rectilinear shear flows. However, the theorem is not applicable for curvilinear geometries such as the Dean/Taylor-Couette configurations, and thence there is no real contradiction. The extent of decrease in Wi_c for $\epsilon = 1$ (from 227.76 for $\alpha = 0$ to 202.03 for $\alpha = 1.3$) is, however, not substantial, and Wi_c for $\alpha = 0$ serves therefore as a reasonably accurate estimate for the true threshold (obtained by minimizing over both n and α). Thus, for the CM instability, in the ensuing discussion, we present the critical Wi_c obtained for two-dimensional disturbances.

Figure 14(a) shows the reduction in Wi_c with increasing ϵ , for different β 's; representative data, corresponding to this figure, is given in Table 3 for completeness. Figure 14(b) shows the variation of the critical Weissenberg number Wi_c with $(1 - \beta)$, for different ϵ . The CM instability is seen to be restricted to $\beta \geq 0.99$ for $\epsilon \leq 0.1$, consistent with the β -threshold of 0.9905 for plane Poiseuille flow (Khalid *et al.* 2021b). The instability must clearly be absent for $\beta = 1$, and we indeed find that Wi_c diverges as $(1 - \beta)^{-1}$ for $\beta \rightarrow 1$. Further, the unstable interval of β 's increases with increasing ϵ , implying that the instability is present over a larger range of polymer concentrations as domain curvature becomes important. Interestingly, the crossing of the different curves in Fig. 14(a) shows that, in addition to the increase in the unstable β -interval, it is the smallest β 's that become the most unstable with increasing ϵ , in terms of having the smallest Wi -thresholds - this is consistent with both the widening and lowering of the unstable region in Fig. 14(b).

4.2. Role of finite extensibility on CM in Dean flow

To begin with, in Fig. 15, we present the elastic spectrum for the FENE-P fluid with $L = 100$ and $\beta = 0.98$, focusing on two-dimensional disturbances. Interestingly, the CM is unstable here, even at a relatively lower $Wi = 60$. The effect of decreasing L on the CM has been shown to be quite subtle in the case of pressure-driven rectilinear channel flow (Khalid *et al.* 2025), in that it could be uniformly stabilising or destabilising, or even non-monotonic; we find a similar trend for Dean flow below. The effect of introducing axial variation was also investigated for $L = 100$ and we again found (data not shown) a slight destabilization as α is increased up to approximately 1; however, a further increase in α leads to stabilization, similar to the Oldroyd-B case discussed above (Fig. 13(a)).

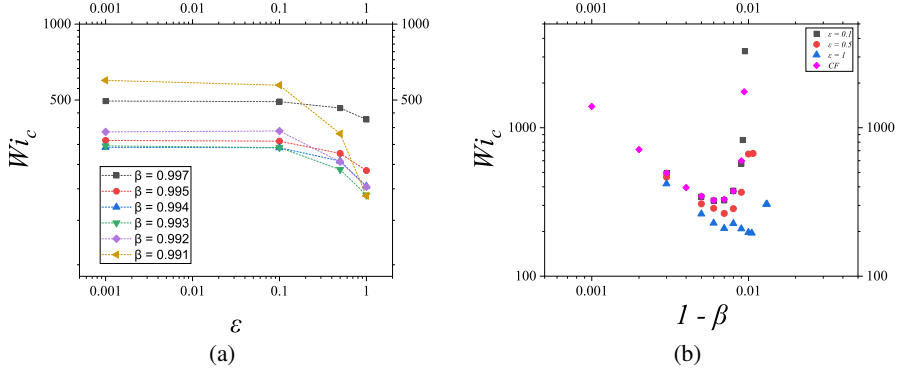


Figure 14: The centre-mode instability in Dean flow of an Oldroyd-B fluid at $Re = 0$, $\alpha = 0$: (a) Variation of critical Weissenberg number (Wi_c) with ϵ at different β 's; (b) Variation of Wi_c with $(1 - \beta)$ at different ϵ . Here 'CF' represents the results for plane Poiseuille flow (Khalid *et al.* 2021b).

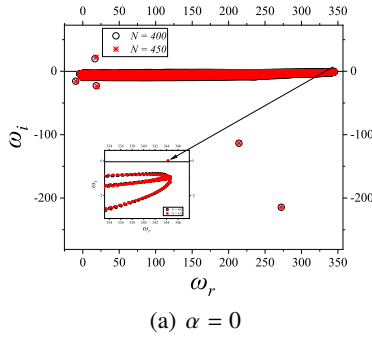


Figure 15: Eigenspectrum showing the presence of unstable centre mode in Dean flow of a FENE-P fluid (with $n = 40$, $\epsilon = 0.1$, $\beta = 0.98$, $L = 100$ and $Wi = 60$). The insets show the zoomed-in view highlighting the region near the unstable centre mode; the discrete eigenvalues obtained for $N = 400$ and $N = 450$ show good convergence.

Khalid *et al.* (2025) first showed, for plane Poiseuille flow, that the neutral curves, for the FENE-P model, form closed loops in the $Wi-k$ plane, as opposed to the open tongues (enclosing the unstable region) seen earlier in Fig. 11 for the Oldroyd-B case. The closing out of the tongues, leading to loops, is a manifestation of the expected stabilizing role of shear thinning, mentioned earlier in Sec. 1.1, and which results in a weakening of elastic effects at sufficiently high Wi 's. As shown in Fig. 16(a), in Dean flow too, the neutral curves are closed loops in the $Wi-n$ plane. Importantly, the destabilizing effect of curvature (i.e., increasing ϵ) persists for the FENE-P model as well, as evident from the neutral loops in Fig. 16(a) shifting downward when ϵ is increased to $O(1)$ values. We also find very good agreement between the loop for $\epsilon = 0.01$ with the one obtained by Khalid *et al.* (2025) for pressure-driven channel flow. Furthermore, as shown in Fig. 16(b), the destabilizing effect of L on the CM, originally predicted for pressure-driven channel flow (Page *et al.* 2020; Khalid *et al.* 2025), persists even for Dean flow at finite ϵ . Indeed, an obvious signature of the finite-extensibility-induced destabilization is the fact that we continue to get unstable islands even for $\beta = 0.98$ in Fig. 16(a); the flow is stable for the Oldroyd-B model for this β .

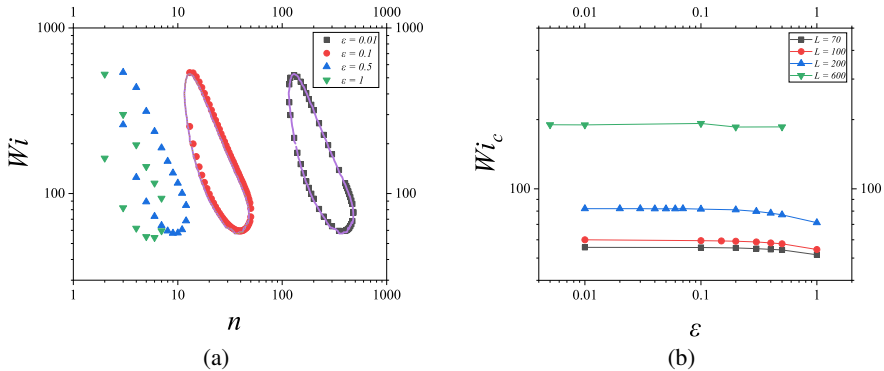


Figure 16: Centre-mode instability in Dean flow of a FENE-P fluid: (a) Neutral curves at different ϵ 's for $L = 100$. For $\epsilon = 0.01$ and 0.1 , we also plot the neutral curve (continuous lines) obtained for pressure-driven flow in a rectilinear channel (Khalid *et al.* 2025); (b) Variation of Wi_c with ϵ at different L 's. Data for both panels correspond to $Re = 0$, $\alpha = 0$, and $\beta = 0.98$.

In Appendix C, we demonstrate that the CM instability is not governed solely by the ratio Wi/L (for different (Wi, L) pairs), although the base state profiles are, as was demonstrated in Sec. 2.3. The eigenfunctions for various field variables corresponding to the CM in Dean flow (for $L = 100$ and $\epsilon = 0.1$) are shown in Appendix D by way of comparison with those for the HSM. While the key features of the CM eigenfunctions are rather robust to changes in ϵ and L , they are qualitatively different from the corresponding HSM eigenfunctions.

5. Elastic hoop-stress instability in Dean flow

As mentioned in the Introduction, previous efforts by Joo & Shaqfeh (1991, 1994) have characterized, using the Oldroyd-B model, the hoop-stress-induced elastic instability in Dean flow. Here, we use the more general FENE-P model and examine the role of finite extensibility on the HSM. As evident from Figs. 4 and 7 of Sec. 3, the Oldroyd-B model predicts both axisymmetric (stationary or propagating, depending on α) and non-axisymmetric (propagating) modes to turn unstable on account of a well-known hoop-stress mediated mechanism. The neutral curves for this case were already seen in Fig. 3, in the narrow-gap limit, in the context of the validation exercise. The comparison between the axisymmetric and non-axisymmetric thresholds is shown in Figs. 17(a) and 17(b), which plot the neutral curves for $\epsilon = 0.1$ and 1 , respectively. For both ϵ 's, the axisymmetric mode is the most critical, consistent with the earlier efforts of Joo & Shaqfeh (1991, 1994). A distinct kink is observed in the associated neutral stability curves (at both ϵ 's shown), owing to the bifurcation from stationary to propagating modes.

Recall from the discussion in Sec. 1 that, for $\epsilon \ll 1$, the critical Weissenberg number (Wi_c) diverges as $\epsilon^{-1/2}$ for the axisymmetric mode. Accordingly, in Fig. 18(a), $\epsilon^{1/2}Wi_c$ is almost independent of ϵ , until $\epsilon \approx 0.1$. This is followed by a mild increase in $\epsilon^{1/2}Wi_c$ as ϵ is increased from 0.1 to 1 . Note that, unlike the CM instability, which is present only for $\beta > 0.99$ in plane Poiseuille flow within the Oldroyd-B framework (we note, however, that the CM instability has been shown to exist in Kolmogorov flow even for $\beta \rightarrow 0$ by Lewy & Kerswell 2025), the hoop-stress mode (HSM1) is present even in the absence of solvent ($\beta = 0$), as was indeed already evident from Fig. 3. However, both instabilities must cease to exist for $\beta \rightarrow 1$. The critical Wi_c for the HSM diverges as $(1 - \beta)^{-1/2}$ in this limit - Fig. 18(b) shows that this

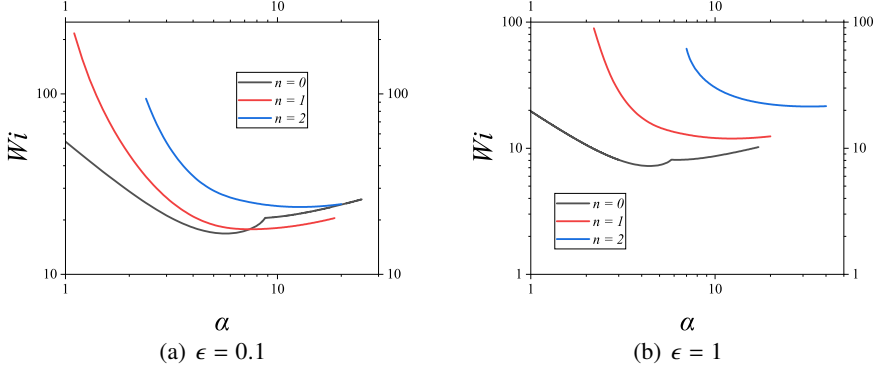


Figure 17: HSM1 neutral curves for both axisymmetric and non-axisymmetric disturbances at different ϵ 's. Data for the Oldroyd-B model ($Re = 0$ and $\beta = 0.98$).

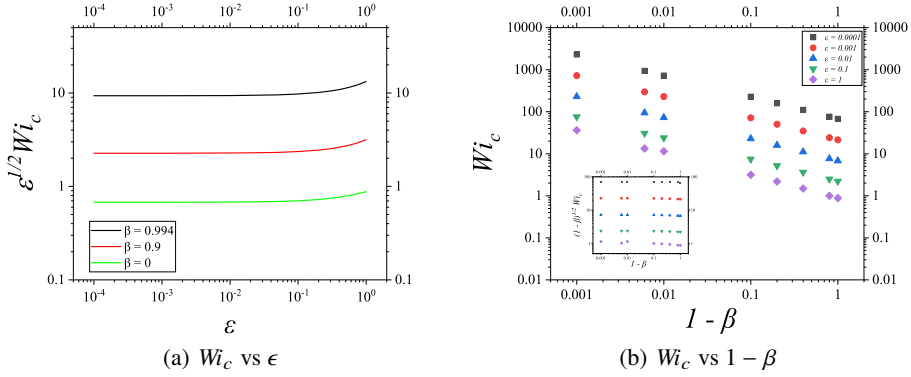


Figure 18: Critical Weissenberg number (Wi_c) for HSM1 in Dean flow of an Oldroyd-B fluid at $Re = 0$ and $n = 0$: (a) $\epsilon^{1/2} Wi_c$ as a function of ϵ for various values of β ; (b) Wi_c as a function of $1 - \beta$ for different gap width ratios ϵ ; the inset shows $(1 - \beta)^{1/2} Wi_c$ remains approximately a constant as β is varied.

scaling continues to hold for any $\beta \in [0, 1)$. The scaling can be anticipated from the Pakdel-McKinley argument (Eq. 1.1) as follows. Using $\mathcal{R} = R_1$, $N_1 \propto \lambda \eta_p (U_m/d)^2$, and the total shear stress $|\tau| \propto \eta U_m/d$ in the PM criterion, we obtain

$$\frac{\lambda U_m}{R_1} \frac{\lambda \eta_p (U_m/d)^2}{\eta U_m/d} \geq O(1). \quad (5.1)$$

Upon using $\epsilon = d/R_1$, and $\eta_p/\eta = (1 - \beta)$, the above equation becomes

$$\left(\frac{\lambda U_m}{d} \right)^2 \epsilon (1 - \beta) \geq O(1), \quad (5.2)$$

which yields $Wi_c \geq (\epsilon(1 - \beta))^{-1/2}$; note that the divergence exponent $-1/2$ applies to both ϵ and $(1 - \beta)$. In contrast, Wi_c for the centre mode obeys an ϵ -independent scaling $Wi_c \sim (1 - \beta)^{-1}$, for $\beta \rightarrow 1$, in the narrow-gap limit (Fig. 14(b)), with this being followed by a rapid increase and divergence at a (slightly lower) threshold $\beta \approx 0.99$.

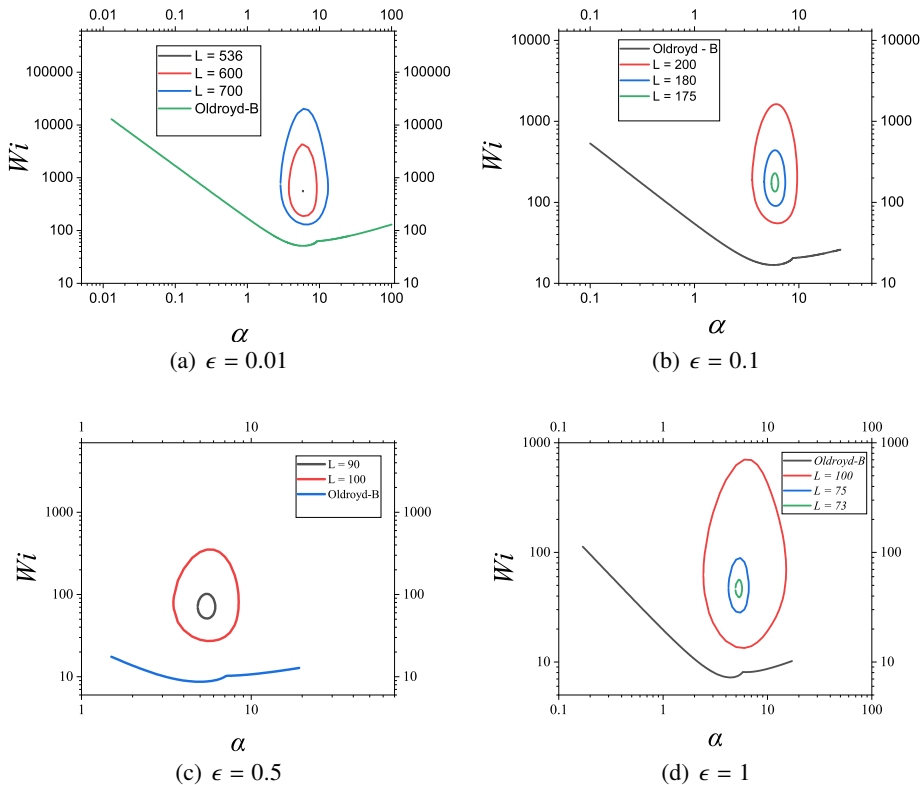


Figure 19: Neutral curves for HSM1 in the Wi - α plane for Dean flow of a FENE-P fluid at $Re = 0$, $\beta = 0.98$, $n = 0$.

5.1. Role of finite extensibility on axisymmetric modes

In Fig. 19, we show the neutral curves for HSM1 (the most critical mode in the Oldroyd-B model) in the Wi - α plane for L 's ranging from the Oldroyd-B limit down to 100. The eigenspectra corresponding to these neutral curves were presented in Fig. 6. Owing to the stabilising role of finite extensibility, the neutral stability curves for finite L are again closed loops in the Wi - α plane for the entire range of gap width ratios examined, analogous to the neutral loops for CM in Fig. 16(a). Similar closing out of the neutral curves due to shear-thinning-induced weakening of the first normal stress difference has been demonstrated using the Giesekus (Oztekin *et al.* 1994) and FENE-CR (McKinley *et al.* 1995) models for the hoop-stress instability for flow in the cone-and-plate geometry. Unlike the Oldroyd-B model, which exhibits a kink due to a transition from stationary to propagating modes, for the L 's shown in Fig. 19, the transition to instability occurs via propagating modes for all the ϵ 's considered in this figure.

For Dean flow considered in this effort, the shear-thinning-induced stabilization, as expected, is strongest for the smallest ϵ ($= 0.01$), owing to the high Wi – the loop in Fig. 19(a) already being vanishingly small at $L = 536$. In contrast, for $\epsilon = 0.1$, the loop remains finite in extent, even for $L = 175$. This sensitivity to ϵ is further highlighted in Fig. 20, where we show neutral stability loops in the Wi - α plane for $L = 100$, over a range of ϵ 's. The size of the unstable region decreases with decreasing ϵ , for the said L , with the HSM being absent

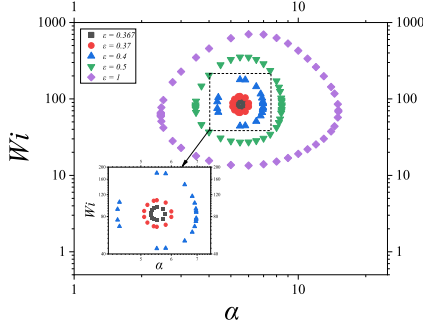


Figure 20: Neutral curves for HSM1 at different ϵ 's showing the absence of HSM1 for $\epsilon \lesssim 0.36$. Data for $Re = 0$, $n = 0$, $\beta = 0.98$ and $L = 100$. The inset shows an enlarged view of the region $40 < Wi < 200$.

for $\epsilon \lesssim 0.36$. For smaller ϵ 's, it is necessary to further examine modes with $n \neq 0$ in order to ascertain the presence of an HSM instability, which we do in the next subsection.

5.2. Role of finite extensibility on non-axisymmetric modes

To begin with, we recall the discussion in Sec. 3.2 which had identified HSM2, a second discrete mode in the elastic spectrum, besides the dominant one (HSM1) that governed the transition for the Oldroyd-B case. Herein, we examine HSM1 and HSM2 for the FENE-P case in more detail. Thus, while Fig. 7(b) was for $L = 200$, Fig. 21 examines the non-axisymmetric spectrum ($n = 1$) for L decreasing from 10^6 (the Oldroyd-B limit for all practical purposes) down to 100. Decreasing L has a stabilising effect on HSM1, as one might anticipate from the stabilising role of shear thinning on the hoop-stress instability mentioned in our earlier discussion. Rather intriguingly, for HSM2, decreasing L has an initial destabilizing effect, although an ultimately stabilizing one. This destabilising influence of finite extensibility on HSM2 is reminiscent of its effect on the centre mode in plane channel flow (Buza *et al.* 2022b; Khalid *et al.* 2025), and in Dean flow (as discussed in Sec. 4.2). However, HSM2 is not a centre mode, and has more in common with HSM1, in terms of the trends shown by its eigenfunctions - this is demonstrated in Appendix D which compares the eigenfunctions for HSM1, HSM2, and CM. Figure 22 shows the variation of the growth rate (ω_i) with L for both HSM1 and 2 (for $n = 2$), with Fig. 22(b) presenting a magnified view of the region $50 < L < 10^3$. The non-monotonic variation of ω_i for HSM2 is evident in Fig. 22(a) and is in contrast to the behaviour of HSM1. This leads to HSM1 being the critical mode for $L > 200$, and HSM2 being critical for $L < 200$. Indeed, for $L = 100$, the only unstable mode in the spectrum is HSM2, with the classical hoop-stress mode (HSM1) being completely stabilised. An identical scenario prevails for $n = 1$ (not shown).

For the FENE-P case, the destabilizing influence of finite extensibility on both CM and HSM2 might lead one to anticipate that these two modes might be connected in some regions of the parameter space. Figure 23 shows that this is not the case. This figure shows the neutral curves for HSM2 and CM, in the Wi - α plane, for both Oldroyd-B and FENE-P ($L = 100$) fluids, for $\epsilon = 1$. For the Oldroyd-B fluid, while the CM is stable for $\alpha = 0$ (when $\beta = 0.98$), the CM is destabilized by nonzero α . In addition, there are neutral curves related to HSM1 and 2; in this figure, we do not show the HSM1 neutral curve for $n = 2$. The critical Wi for the $n = 2$ mode in the FENE-P ($L = 100$) model is significantly higher than that for the Oldroyd-B case, due to the stabilising influence of finite extensibility. The unstable region for HSM2 (with $n = 2$) is completely disconnected from the CM, both for Oldroyd-B and FENE-P

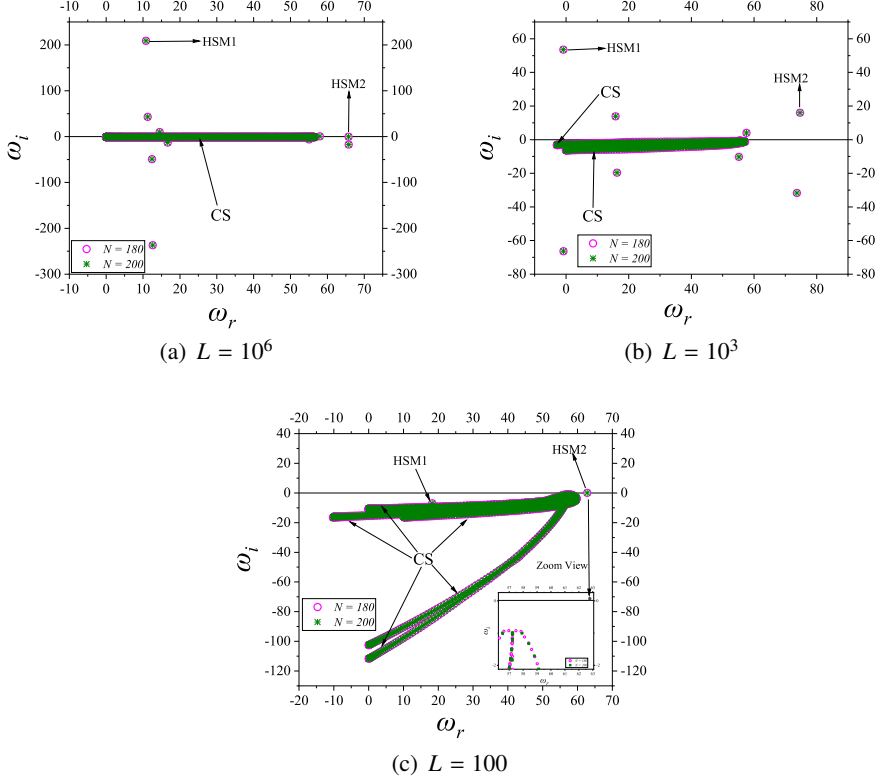


Figure 21: Eigenspectra showing HSM1 and 2 in Dean flow of a FENE-P fluid at $Re = 0$, $\alpha = 7$, $\beta = 0.98$, $\epsilon = 0.1$, $n = 1$, $Wi = 400$ at different L 's. The continuous spectra are indicated as 'CS'.

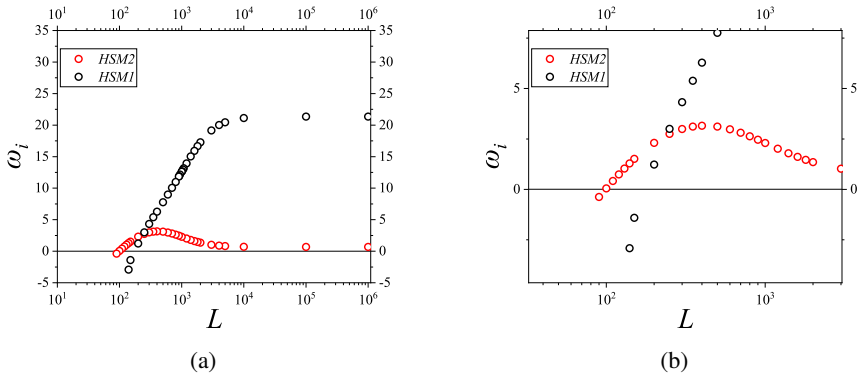


Figure 22: Variation of ω_i with L for the hoop stress modes (HSM1 and HSM2) in Dean flow of a FENE-P fluid for $\epsilon = 0.1$, $\alpha = 7$, $n = 2$, $Re = 0$, $Wi = 130$, and $\beta = 0.98$: (a) for $10 < L < 10^6$, and (b) zoomed-in view of (a) highlighting the crossover from HSM1 to HSM2.

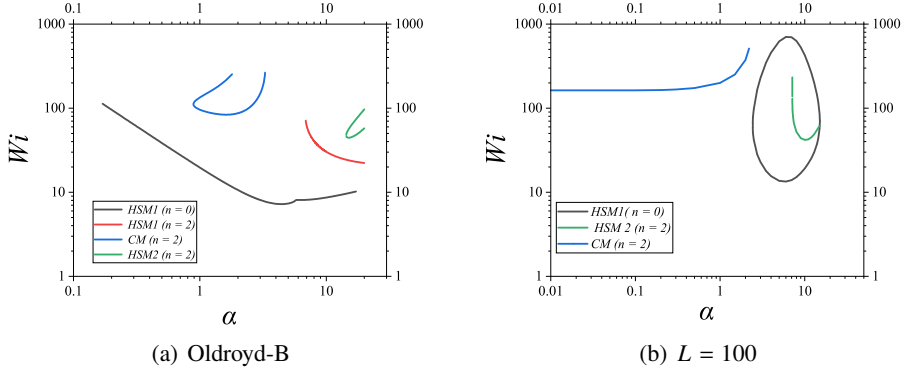


Figure 23: Neutral curves for CM and non-axisymmetric HSM2 for the Oldroyd-B and FENE-P ($L = 100$) models. Data for $n = 2$, $Re = 0$, $\epsilon = 1$, $\beta = 0.98$. The results for axisymmetric HSM1 are shown for reference.

fluids. As α is increased for a fixed Wi (in Fig. 23), we find that the CM becomes stable and eventually merges into the CS, a trend that is reminiscent of the CM in rectilinear channel and pipe flows (Chaudhary *et al.* 2021; Khalid *et al.* 2021a). Similarly, when we tracked HSM2 for a Wi from the unstable region, the ω_r for this mode is such that it is beyond the CS range, and hence this mode circumvents the CS and eventually ends up below it, without crossing the same. This shows that the two modes (HSM2 and CM) do not continue to each other, as α is varied for a fixed Wi . While the above discussion pertains to HSM2 and CM, it is relevant to emphasise that for the larger gap-width ratio of $\epsilon = 1$, the HSM1 (with $n = 0$) is the most critical for both the Oldroyd-B and FENE-P models.

As mentioned in Sec. 5, for the Oldroyd-B case, the axisymmetric HSM1 is the most unstable mode for any ϵ . However, the trend is very different for the FENE-P case, being sensitive to the choice of ϵ and L . For $L \sim 100$, the nature of the most unstable mode (viz., axisymmetric vs. non-axisymmetric HSM2) depends on ϵ , as shown in Fig. 24. In the narrow-gap regime ($\epsilon = 0.01 - 0.2$), the axisymmetric modes (both HSM1 and 2) remain stable for $L = 100$, while a non-axisymmetric HSM2 becomes critical. Specifically, at $\epsilon = 0.1$, $n = 2$ is the critical mode (HSM2), whereas at $\epsilon = 0.2$, $n = 1$ emerges as the critical mode (HSM2). In contrast, for the larger values $\epsilon = 0.5$ and 1, the axisymmetric (HSM1) mode becomes critical. Notably, the range of ϵ 's between 0.1 and 0.3 corresponds to gap widths used in the Taylor-Dean experiments of (Joo & Shaqfeh 1994), although the serpentine channel experiments of Groisman & Steinberg (2001, 2004) used a higher $\epsilon = 1$; we return to this issue in Sec. 6.

For the Oldroyd-B model, the critical Weissenberg number (Wi_c) was seen to scale as $\epsilon^{-1/2}$ for $\epsilon \ll 1$. In contrast, and as demonstrated in Figs. 19 and 24, one expects the HSM instability to be fully suppressed for $\epsilon \rightarrow 0$, as L is decreased. This is illustrated in Fig. 25(a), where the critical Wi_c is seen to diverge faster than $\epsilon^{-1/2}$ for all finite L . Note that the data points in Fig. 25(a) for Wi_c (at different ϵ 's or L 's) could correspond to either HSM1 ($n = 0$), or HSM1 ($n \neq 0$), or HSM2 ($n \neq 0$). Importantly, as L is decreased to realistic values ~ 100 , the HSM1 is fully suppressed in Dean flow, with a suggestion of divergence at a finite ϵ . This result is in qualitative agreement with what one obtains at a scaling level by incorporating shear thinning in the Pakdel-McKinley criterion (see Fig. 15 of Castillo Sánchez *et al.* 2022). Figure 25(b) shows the critical azimuthal wavenumber n_c as function of ϵ at different L 's; the notation used is similar to Fig. 25(a), in that open symbols pertain to HSM1, while filled

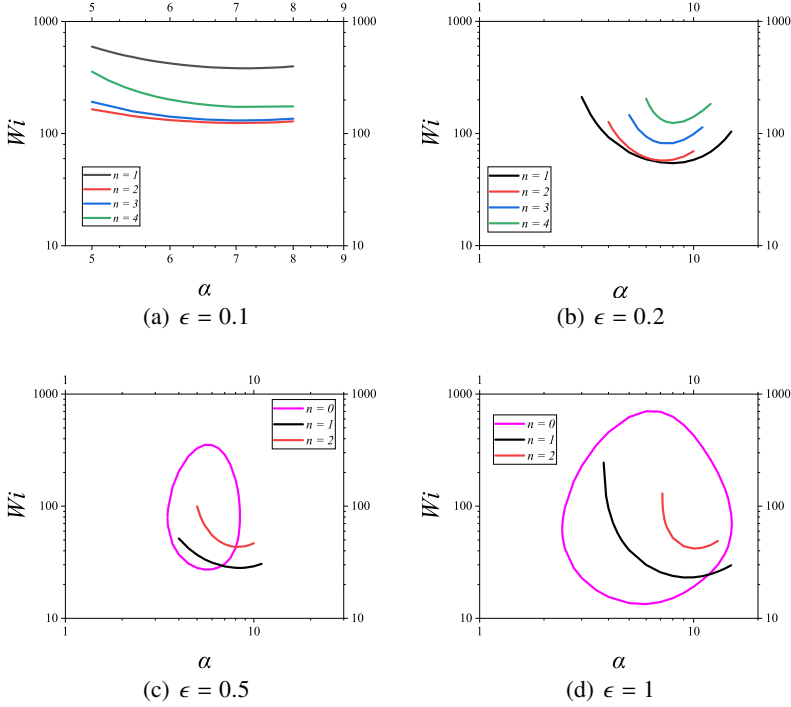


Figure 24: Neutral curves for HSM (1 and 2) at $Re = 0$, $\beta = 0.98$ and $L = 100$. While the $n \neq 0$ modes (HSM2) are the most unstable for $\epsilon = 0.1$ and 0.2 , and remain unstable even for $\epsilon = 0.5$ and 1 , the $n = 0$ mode (HSM1) becomes critical at $\epsilon = 0.5$ and 1 .

symbols to HSM2. While in the Oldroyd-B limit, $n = 0$ always remains critical for all ϵ 's, the critical azimuthal wavenumber for lower L 's changes with ϵ , and there does not appear to be a simple trend. Figure 25(c) shows the corresponding critical axial wavenumber α_c . The abrupt variation of α_c with ϵ in this figure is on account of the transition from HSM1 to HSM2, and also due to changes in n_c .

6. Conclusions

Elastic instabilities in the absence of fluid inertia have traditionally been associated with curvilinear shear flows (Pakdel & McKinley 1996), driven by hoop stresses induced by streamline curvature. Recently, Khalid *et al.* (2021b) identified a novel centre-mode (CM) elastic instability in rectilinear viscoelastic channel flow, driven by a mechanism that is not reliant on streamline curvature, and analogues of which have subsequently been found in other rectilinear shearing flows (Priyadarshi *et al.* 2023; Yadav *et al.* 2024; Lewy & Kerswell 2025). In this study, for the first time, we have shown the presence of both hoop-stress (HSM) and centre-mode (CM) instabilities in the same shearing flow, the Dean flow configuration, using both Oldroyd-B and FENE-P models. While Dean flow approaches plane Poiseuille flow in the narrow-gap limit (with $\epsilon \rightarrow 0$), thence guaranteeing the presence of a CM instability in the narrow-gap limit, as argued below, the CM turns out to be the most unstable mode for realistic values of $L \sim 100$ in the FENE-P model even for experimentally relevant ϵ 's (≈ 0.1 – 0.3). Thus, the present study demonstrates the importance of two qualitatively distinct

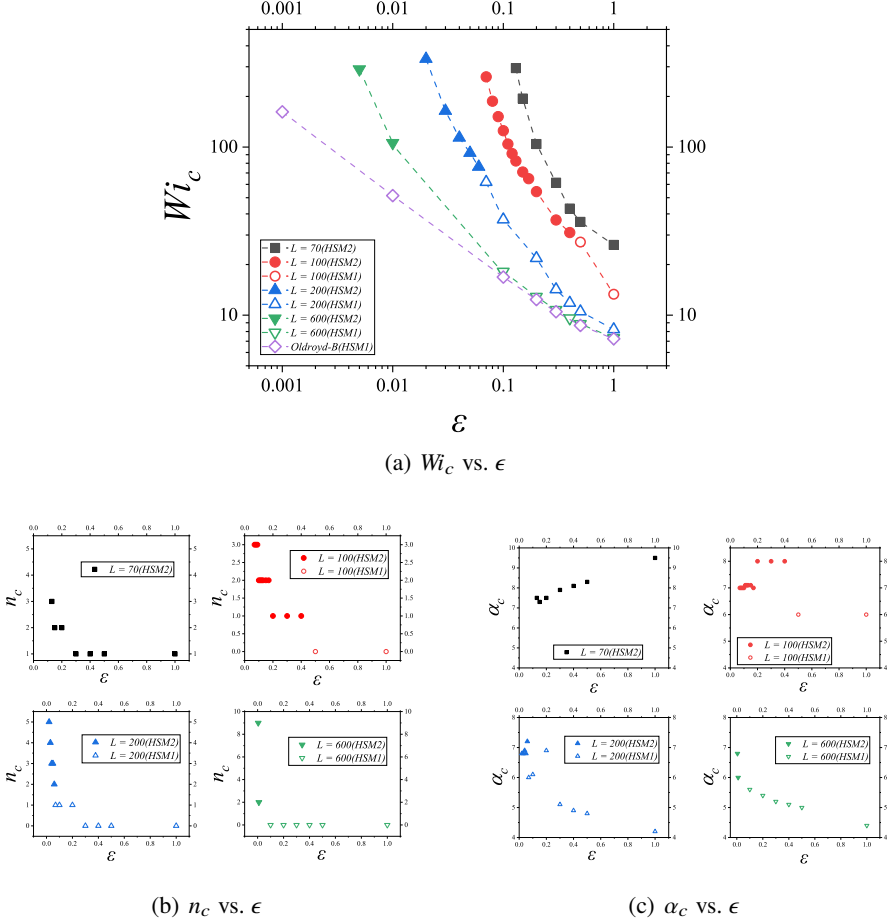


Figure 25: (a) Wi_c vs. ϵ for HSM (1 and 2) in Dean flow at different L 's illustrating the stabilising influence of finite extensibility. Here, filled symbols of a given shape denote HSM2 and the corresponding open ones denote HSM1; different symbol shapes corresponds to different L 's. Panels (b) and (c) show the corresponding n_c and α_c variation with ϵ . Data for $Re = 0$ and $\beta = 0.98$.

elastic instabilities in the same curvilinear flow configuration, and thence, the possibility of two different routes to an eventual (elastic) turbulent regime.

It is useful to compare the critical Wi_c for each of these modes in order to determine which one is more critical, and as to how the criticality is influenced by ϵ and L . On account of the existence of the CM instability only in the dilute limit, in the inertialess regime, the ensuing discussion applies only for $\beta > 0.95$; although, as discussed below, nonlinear stability considerations will likely render the CM significant over a wider range of β (Buza *et al.* 2022a). Figure 26 shows that, within the Oldroyd-B framework ($L \rightarrow \infty$), the axisymmetric HSM is the more unstable mode across all experimentally reasonable gap width ratios, viz., $\epsilon \geq 0.1$. As a result, although the range of β 's over which the CM is unstable is slightly larger than that for pressure-driven channel flow, this is of little consequence within the Oldroyd-B framework.

Figure 27 shows the HSM and CM thresholds as a function of ϵ , for different L 's, for $\beta = 0.98$. Figure 27(a) suggests that the CM instability is not relevant for $L = 600$; for the

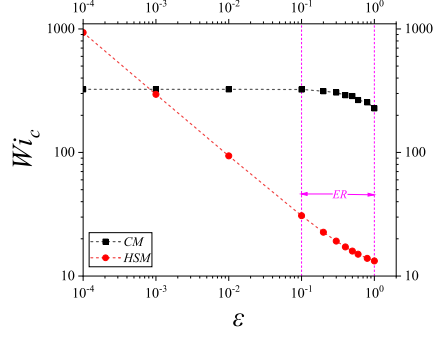
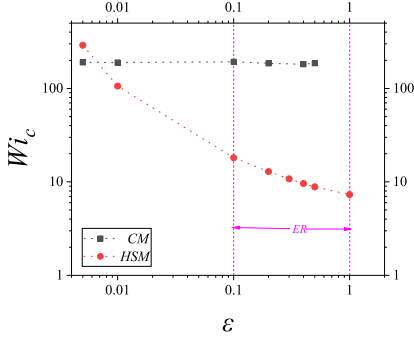
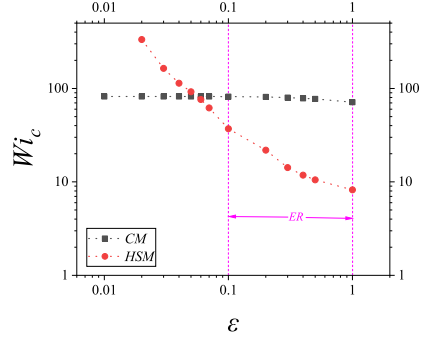


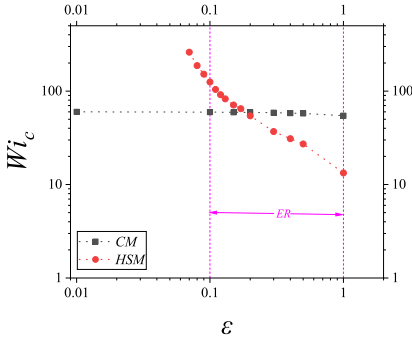
Figure 26: For the Oldroyd-B fluid, the CM becomes the critical mode only for $\epsilon < 10^{-3}$; for $\epsilon > 10^{-3}$, HSM is more unstable. Data showing the variation of Wi_c with ϵ for $Re = 0$ and $\beta = 0.994$. The range indicated by ‘ER’ denotes the ϵ ’s typically used in experiments involving Taylor-Couette and Taylor-Dean configurations.



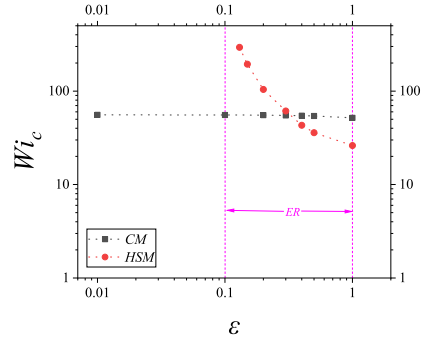
(a) $L = 600$



(b) $L = 200$



(c) $L = 100$



(d) $L = 70$

Figure 27: For Dean flow of FENE-P fluids, as L is decreased, the CM remains more critical compared to HSM at increasingly higher ϵ ’s. Data showing Wi_c vs ϵ at $\beta = 0.98$, $Re = 0$. The range indicated by ‘ER’ denotes the ϵ ’s typically used in experiments.

polyacrylamide solutions routinely used in experiments, $L \sim 600$ would imply a molecular weight of $\gtrsim 10^8$ g/mol. However, the highest molecular weight used hitherto in experiments probing elastic instabilities is 1.8×10^7 g/mol (e.g., see [Neelamegam *et al.* 2013](#)). The CM starts to become relevant for $L = 200$, and is certainly the only one present for $\epsilon \leq 0.1$ and $L < 100$ (as appropriate for the polyacrylamide solutions used in [Choueiri *et al.* 2021](#), with a molecular weight of 5×10^6 g/mol). For the latter range of L , as shown in Fig. 27(c), the CM is the most critical mode for $\epsilon = 0.1$ – 0.3 corresponding to the Taylor-Dean experiments of [Joo & Shaqfeh \(1994\)](#), although the HSM will likely be dominant in the serpentine channel experiments of [Groisman & Steinberg \(2004\)](#) with $\epsilon = 1$. To a good approximation, the critical Wi_c is obtained by setting $\alpha = 0$, implying that the critical mode is nearly two-dimensional. It is worth adding that, although the focus of this work is on Dean flow, most of the results are expected to carry over to the Taylor-Dean geometry as well, in light of a similar demonstration for CM in Couette-Poiseuille flows in a rectangular channel ([Yadav *et al.* 2024](#)). Thus, in experiments involving the Dean or Taylor-Dean configurations, for realistic values of ϵ and L , the CM instability will be relevant for sufficiently dilute solutions such that $\beta > 0.95$, while the HSM is expected to be the dominant mode for $\beta < 0.95$; at least within the linear stability framework. Crucially, the demonstration by [Buza *et al.* \(2022a\)](#), of finite-amplitude travelling waves borne out of the elastic CM instability in rectilinear channel flow being strongly subcritical and existing at $Wi \lesssim 50$ and for β down to 0.7 , suggests that the centre mode could be relevant even in parameter regimes where it is linearly stable in Dean flow.

Finally, even in parameter regimes where the CM is critical, it is tempting to speculate that the primary CM instability will essentially act to modify and augment the streamline curvature in Dean flow, which could then be susceptible to a secondary instability, driven by the hoop-stress mechanism, involving spanwise perturbations. While a similar scenario has been earlier proposed by Morozov and coworkers ([Morozov & van Saarloos 2005a,b, 2019](#)) for rectilinear viscoelastic flows in parametric regimes devoid of any linear instability, the above proposal is actually closer in spirit to the three-dimensional secondary instability in (Newtonian) boundary-layer flows, as demonstrated by [Herbert \(1988\)](#). In the latter context, the Tollmien-Schlichting (TS) mode underlies the primary instability, which then modifies the base flow. This spatially periodic perturbed base state, comprising a superposition of the original boundary-layer flow and a finite amplitude TS mode, subsequently becomes unstable to three-dimensional perturbations.

The demonstration of an analogous secondary instability, for the Dean flow configuration, in regimes where the CM controls the primary transition, will be an interesting avenue for future investigation.

Declaration of interests. The authors report no conflict of interest.

Author contributions. V.S. and G.S. proposed and designed the research. P.S.D.S.P.T. and V.S. derived the equations and developed the code. P.S.D.S.P.T. carried out the simulations. All authors contributed equally to analysing data, reaching conclusions, and writing the paper.

Author ORCIDs. V. Shankar, <https://orcid.org/0000-0003-0233-7494>,
G. Subramanian, <https://orcid.org/0000-0003-4314-3602>

Appendix A. Linearized stability equations for the Oldroyd-B model

The linearized continuity, momentum, and constitutive equations for the Oldroyd-B model are given in this Appendix. Here, and in what follows, $D \equiv \frac{d}{dy}$. Continuity equation:

$$\frac{d\tilde{v}_r}{dy} + \frac{\epsilon}{1 + \epsilon y} \tilde{v}_r + \frac{i\epsilon}{1 + \epsilon y} \tilde{v}_\theta + i\alpha \tilde{v}_z = 0, \quad (\text{A } 1)$$

r -momentum equation:

$$G\tilde{v}_r + G_1\tilde{v}_\theta = -D\tilde{p} + \beta M\tilde{v}_r + M_1\tilde{\tau}_{rr} + M_2\tilde{\tau}_{r\theta} + i\alpha\tilde{\tau}_{rz} - \left(\frac{\epsilon}{1+\epsilon y}\right)\tilde{\tau}_{\theta\theta}, \quad (\text{A } 2)$$

θ -momentum equation:

$$G\tilde{v}_\theta + G_2\tilde{v}_r = -M_2\tilde{p} + \beta M\tilde{v}_\theta + (M_1 + \frac{\epsilon}{1+\epsilon y})\tilde{\tau}_{r\theta} + M_2\tilde{\tau}_{\theta\theta} + i\alpha\tilde{\tau}_{\theta z}, \quad (\text{A } 3)$$

z -momentum equation:

$$G\tilde{v}_z = -i\alpha\tilde{p} + \beta M\tilde{v}_z + M_1\tilde{\tau}_{rz} + M_2\tilde{\tau}_{\theta z} + i\alpha\tilde{\tau}_{zz}, \quad (\text{A } 4)$$

τ_{rr} equation:

$$\zeta\tilde{\tau}_{rr} = 2(1-\beta)\frac{d\tilde{v}_r}{dy} + 2WiM_2\tilde{v}_r, \quad (\text{A } 5)$$

$\tau_{r\theta}$ equation:

$$\zeta\tilde{\tau}_{r\theta} = Wi\left(U' - \frac{\epsilon}{1+\epsilon y}U\right)\tilde{\tau}_{rr} + P\tilde{v}_r + \left[(1-\beta)(D - \frac{\epsilon}{1+\epsilon y}) + M_2\bar{\tau}_{r\theta}\right]\tilde{v}_\theta, \quad (\text{A } 6)$$

τ_{rz} equation:

$$\zeta\tilde{\tau}_{rz} = [(1-\beta)D + WiM_2\bar{\tau}_{r\theta}]\tilde{v}_z + (1-\beta)i\alpha\tilde{v}_r, \quad (\text{A } 7)$$

$\tau_{\theta\theta}$ equation:

$$\zeta\tilde{\tau}_{\theta\theta} = 2Wi\left(U' - \frac{\epsilon}{1+\epsilon y}U\right)\tilde{\tau}_{r\theta} + \left[2(1-\beta)\frac{\epsilon}{1+\epsilon y} - Wi\left(\bar{\tau}'_{\theta\theta} - \frac{2\epsilon}{1+\epsilon y}\bar{\tau}_{\theta\theta}\right)\right]\tilde{v}_r + F\tilde{v}_\theta, \quad (\text{A } 8)$$

$\tau_{\theta z}$ equation:

$$\zeta\tilde{\tau}_{\theta z} = Wi\left(U' - \frac{\epsilon}{1+\epsilon y}U\right)\tilde{\tau}_{rz} + E\tilde{v}_z + (1-\beta)i\alpha\tilde{v}_\theta, \quad (\text{A } 9)$$

τ_{zz} equation:

$$\zeta\tilde{\tau}_{zz} = 2(1-\beta)i\alpha\tilde{v}_z, \quad (\text{A } 10)$$

where $\zeta = \left[1 - i\omega + Wi\left(\frac{i\epsilon}{1+\epsilon y}\right)U\right]$,

$$G = Re\left(\frac{i\epsilon}{1+\epsilon y}U - \frac{i\omega}{Wi}\right),$$

$$M = \left(D^2 + \frac{\epsilon}{1+\epsilon y}D - \frac{\epsilon^2}{(1+\epsilon y)^2} - \frac{n^2\epsilon^2}{(1+\epsilon y)^2} - \alpha^2\right),$$

$$M_1 = \left(D + \frac{\epsilon}{1+\epsilon y}\right), M_2 = \left(\frac{i\epsilon}{1+\epsilon y}\right), G_1 = -2Re\frac{\epsilon}{1+\epsilon y} + \beta\frac{2i\epsilon^2}{(1+\epsilon y)^2},$$

$$G_2 = Re\frac{\epsilon}{1+\epsilon y} - \beta\frac{2i\epsilon^2}{(1+\epsilon y)^2} + ReU',$$

$$E = [Wi(\bar{\tau}_{r\theta}D + M_2\bar{\tau}_{\theta\theta}) + (1-\beta)M_2], F = \left[2Wi\left(\bar{\tau}_{r\theta}D + M_2\bar{\tau}_{\theta\theta} - \frac{\epsilon}{1+\epsilon y}\bar{\tau}_{r\theta}\right) + 2(1-\beta)M_2\right],$$

$$P = \left[Wi\left(\bar{\tau}_{r\theta}D + M_2\bar{\tau}_{\theta\theta} + \frac{\epsilon}{1+\epsilon y}\bar{\tau}_{r\theta} - \bar{\tau}'_{r\theta}\right) + (1-\beta)M_2\right],$$

No-slip boundary conditions $\tilde{v}_r = 0$, $\tilde{v}_\theta = 0$ and $\tilde{v}_z = 0$ are applicable at both $y = 0$ and $y = 1$.

Appendix B. Linearized stability equations for the FENE-P model

The linearized continuity, momentum, and constitutive equations for the FENE-P model are given in this Appendix.

Continuity equation:

$$\left(D + \frac{\epsilon}{1 + \epsilon y}\right) \tilde{v}_r + \frac{i n \epsilon}{1 + \epsilon y} \tilde{v}_\theta + i \alpha \tilde{v}_z = 0 \quad (\text{B } 1)$$

r -momentum Equation:

$$\begin{aligned} Re \left(-\frac{i \omega}{Wi} + \frac{\bar{v}_\theta i n \epsilon}{1 + \epsilon y} \right) \tilde{v}_r - \frac{2 Re \epsilon \bar{v}_\theta}{1 + \epsilon y} \tilde{v}_\theta = & -\frac{\partial \tilde{p}}{\partial y} + \beta \left(\left(\frac{\partial^2}{\partial y^2} - \frac{\epsilon^2}{(1 + \epsilon y)^2} + \frac{\epsilon}{1 + \epsilon y} \frac{\partial}{\partial y} \right. \right. \\ & \left. \left. - \frac{n^2 \epsilon^2}{(1 + \epsilon y)^2} - \alpha^2 \right) \tilde{v}_r - \frac{2 \epsilon^2 i n}{(1 + \epsilon y)^2} \tilde{v}_\theta \right) \\ & + (1 - \beta) \left(\frac{\partial \tilde{\tau}_{rr}}{\partial y} + \frac{\epsilon}{1 + \epsilon y} \tilde{\tau}_{rr} + \frac{i n \epsilon}{1 + \epsilon y} \tilde{\tau}_{\theta r} \right. \\ & \left. + i \alpha \tilde{\tau}_{zr} - \frac{\epsilon}{1 + \epsilon y} \tilde{\tau}_{\theta \theta} \right) \end{aligned} \quad (\text{B } 2)$$

θ -momentum Equation:

$$\begin{aligned} Re \left(\frac{\partial \bar{v}_\theta}{\partial y} + \frac{\bar{v}_\theta \epsilon}{1 + \epsilon y} \right) \tilde{v}_r + Re \left(\frac{\bar{v}_\theta i n \epsilon}{1 + \epsilon y} - \frac{i \omega}{Wi} \right) \tilde{v}_\theta = & -\frac{i n \epsilon}{1 + \epsilon y} \tilde{p} \\ & + \beta \left(\left(\frac{\partial^2}{\partial y^2} - \frac{\epsilon^2}{(1 + \epsilon y)^2} + \frac{\epsilon}{1 + \epsilon y} \frac{\partial}{\partial y} \right. \right. \\ & \left. \left. - \frac{n^2 \epsilon^2}{(1 + \epsilon y)^2} - \alpha^2 \right) \tilde{v}_\theta + \frac{2 \epsilon^2 i n}{(1 + \epsilon y)^2} \tilde{v}_r \right) \\ & + (1 - \beta) \left(\frac{\partial \tilde{\tau}_{\theta r}}{\partial y} + \frac{\epsilon}{1 + \epsilon y} \tilde{\tau}_{\theta r} \right. \\ & \left. + \frac{i n \epsilon}{1 + \epsilon y} \tilde{\tau}_{\theta \theta} + i \alpha \tilde{\tau}_{z \theta} \right) \end{aligned} \quad (\text{B } 3)$$

z -momentum Equation:

$$\begin{aligned} Re \left(-\frac{i \omega}{Wi} + \frac{\bar{v}_\theta i n \epsilon}{1 + \epsilon y} \right) \tilde{v}_z = & -i \alpha \tilde{p} + \beta \left(\frac{\partial^2 \tilde{v}_z}{\partial y^2} - \frac{\epsilon^2}{(1 + \epsilon y)^2} \tilde{v}_z + \frac{\epsilon}{1 + \epsilon y} \frac{\partial \tilde{v}_z}{\partial y} - \frac{n^2 \epsilon^2}{(1 + \epsilon y)^2} \tilde{v}_z - \alpha^2 \tilde{v}_z \right) \\ & + (1 - \beta) \left(\frac{\partial \tilde{\tau}_{rz}}{\partial y} + \frac{\epsilon}{1 + \epsilon y} \tilde{\tau}_{rz} + \frac{i n \epsilon}{1 + \epsilon y} \tilde{\tau}_{\theta z} + i \alpha \tilde{\tau}_{zz} \right) \end{aligned} \quad (\text{B } 4)$$

C_{rr} equation:

$$\left(\bar{C}'_{rr} - 2 \bar{C}_{rr} D - \frac{2 \bar{C}_{r \theta} i n \epsilon}{1 + \epsilon y} \right) \tilde{v}_r + \left(\frac{\bar{v}_\theta i n \epsilon}{1 + \epsilon y} - \frac{i \omega}{Wi} \right) \tilde{C}_{rr} = -\tilde{\tau}_{rr} \quad (\text{B } 5)$$

$C_{r \theta}$ equation:

$$\begin{aligned} \left(\bar{C}'_{r \theta} - \frac{i n \epsilon}{1 + \epsilon y} \bar{C}_{\theta \theta} \right) \tilde{v}_r + \left(\frac{\epsilon \bar{C}_{rr}}{1 + \epsilon y} - \bar{C}_{rr} \frac{\partial}{\partial y} \right) \tilde{v}_\theta + i \alpha \bar{C}_{r \theta} \tilde{v}_z \\ + \left(\frac{\bar{v}_\theta \epsilon}{1 + \epsilon y} - \bar{v}'_\theta \right) \tilde{C}_{rr} + \left(\frac{\bar{v}_\theta i n \epsilon}{1 + \epsilon y} - \frac{i \omega}{Wi} \right) \tilde{C}_{r \theta} = -\tilde{\tau}_{r \theta} \end{aligned} \quad (\text{B } 6)$$

C_{rz} equation:

$$-i\alpha\bar{C}_{zz}\tilde{v}_r - \left(\bar{C}_{rr}\frac{\partial}{\partial y} + \frac{\bar{C}_{r\theta}in\epsilon}{1+\epsilon y}\right)\tilde{v}_z + \left(\frac{\bar{v}_\theta in\epsilon}{1+\epsilon y} - \frac{i\omega}{Wi}\right)\tilde{C}_{rz} = -\tilde{\tau}_{rz} \quad (B 7)$$

$C_{\theta\theta}$ equation:

$$\begin{aligned} \left(\bar{C}'_{\theta\theta} - \frac{2\epsilon}{1+\epsilon y}\bar{C}_{\theta\theta}\right)\tilde{v}_r + \left(\frac{2\epsilon}{1+\epsilon y}\bar{C}_{r\theta} - \frac{2in\epsilon}{1+\epsilon y}\bar{C}_{\theta\theta} - 2\bar{C}_{r\theta}\frac{\partial}{\partial y}\right)\tilde{v}_\theta \\ + 2\left(\frac{\epsilon}{1+\epsilon y}\bar{v}_\theta - \bar{v}'_\theta\right)\tilde{C}_{r\theta} + \left(\frac{\bar{v}_\theta in\epsilon}{1+\epsilon y} - \frac{i\omega}{Wi}\right)\tilde{C}_{\theta\theta} = -\tilde{\tau}_{\theta\theta} \end{aligned} \quad (B 8)$$

$C_{\theta z}$ equation:

$$-i\alpha\bar{C}_{zz}\tilde{v}_\theta - \left(\bar{C}_{\theta r}\frac{\partial}{\partial y} + \frac{in\epsilon}{1+\epsilon y}\bar{C}_{\theta\theta}\right)\tilde{v}_z + \left(\frac{\epsilon}{1+\epsilon y}\bar{v}_\theta - \frac{\partial\bar{v}_\theta}{\partial y}\right)\tilde{C}_{rz} + \left(\frac{in\epsilon}{1+\epsilon y}\bar{v}_\theta - \frac{i\omega}{Wi}\right)\tilde{C}_{\theta z} = -\tilde{\tau}_{\theta z} \quad (B 9)$$

C_{zz} Equation:

$$\frac{\partial\bar{C}_{zz}}{\partial y}\tilde{v}_r - 2i\alpha\bar{C}_{zz}\tilde{v}_z + \left(\frac{in\epsilon}{1+\epsilon y}\bar{v}_\theta - \frac{i\omega}{Wi}\right)\tilde{C}_{zz} = -\tilde{\tau}_{zz} \quad (B 10)$$

Appendix C. Eigenspectra for viscoelastic Dean flow

In Fig. 28, we present the axisymmetric eigenspectra for the Oldroyd-B fluid at different axial wavenumbers α , for a fixed Wi . As mentioned in Sec. 3.1, for $\beta = 0.98$, the two point CS are nearly overlapping (with $\omega_i = -1$) in this figure. Twelve branches of discrete modes are seen to spread out from the (point) CS, and $\omega_r \neq 0$ for these modes. At lower α 's, we also find two least stable modes which are stationary (i.e. $\omega_r = 0$), with the mode having the higher growth rate turning unstable for $\alpha = 7$. As α is increased further, the aforementioned stationary modes coalesce in a bifurcation, giving rise to symmetrically placed propagating modes (of the form $\pm\omega_r + \omega_i$), with no stationary discrete modes present in the spectrum.

This bifurcation can happen either in the stable ($\omega_i < 0$) or unstable ($\omega_i > 0$) regions of the parameter space; for the Wi chosen in Fig. 28, the bifurcation occurs prior to the instability. For the scaled equations obtained in the narrow-gap limit ($\epsilon \rightarrow 0$, $\epsilon^{1/2}Wi \sim O(1)$), the most unstable mode appears to always remain stationary. Figure 29 depicts the structure of the spectrum for varying Wi , and for α fixed at 7. In this case, the spectrum evolves in the opposite direction (relative to Fig. 28) as Wi is increased from 1.6 to 13; in that, we start off with the pair of least stable modes being propagating ones, which move towards each other with increasing Wi , coalescing at $Wi \approx 13.52$. As Wi is increased further, two stationary modes bifurcate out of the coalescence point, with one of the modes becoming unstable, while the other becomes more stable, viz., they travel in the opposite directions along the $\omega_r = 0$ axis. Although not shown here, we have verified that, for $\epsilon = 0.1$ and $\beta = 0.98$, the least stable modes are stationary at all Wi for $\alpha < \alpha_{\text{critical}} \approx 4$. In contrast, for $\alpha > \alpha_{\text{critical}} = 4$, the least stable modes are propagating at lower Wi (e.g., $Wi = 1.6$), but eventually become stationary at higher Wi .

The effect of increasing Wi/L on the spectra is shown in Fig. 30; this may be achieved by increasing Wi for a fixed L (as in the figure), or by decreasing L for a fixed Wi . Here, the two symmetrically placed wing-like structures as well as the vertical line-like segments on the imaginary axis (as discussed in Sec. 3) are numerical approximations of the CS in Dean flow (Mohanty *et al.* 2025). The spectrum approaches a purely continuous one as Wi is increased

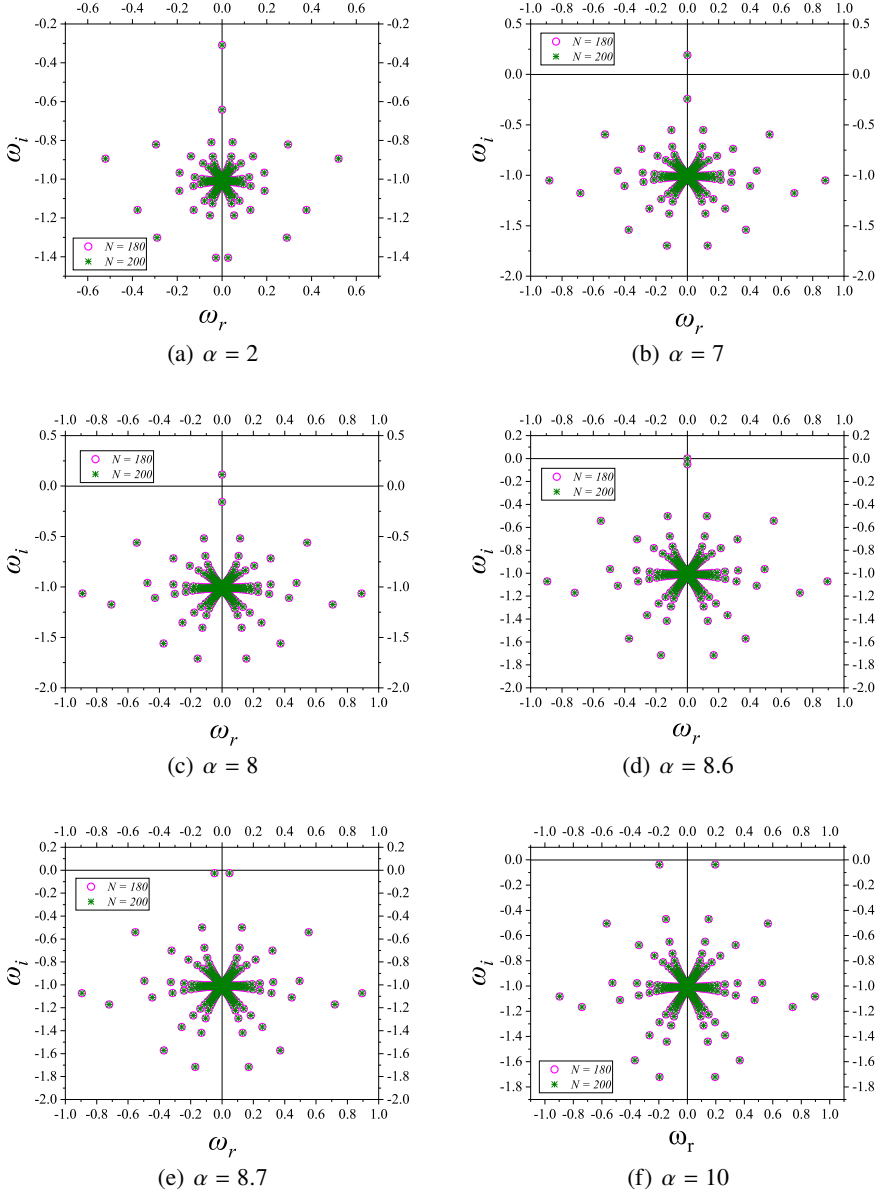


Figure 28: Axisymmetric ($n = 0$) eigenspectra for different α at $Wi = 20$, $\epsilon = 0.1$, $\beta = 0.98$ for Dean flow of an Oldroyd-B fluid demonstrating the bifurcation of stationary HSM into two propagating modes.

from Fig. 30(a) - 30(f), with the wings in particular assuming their full form for the largest Wi/L .

Figures 31(a) and 31(c) depict the spectra for the same Wi/L , albeit at different choices of Wi and L ; Figs. 31(b) and 31(d) show their corresponding magnified views. A data collapse of the base-state velocity profiles was demonstrated for different pairs of (Wi, L) for a fixed Wi/L ratio for Dean flow for fixed ϵ and β (see Fig. 2). However, Fig. 31 shows that the eigenspectrum is independently influenced by Wi and L , and not just by the Wi/L alone. This

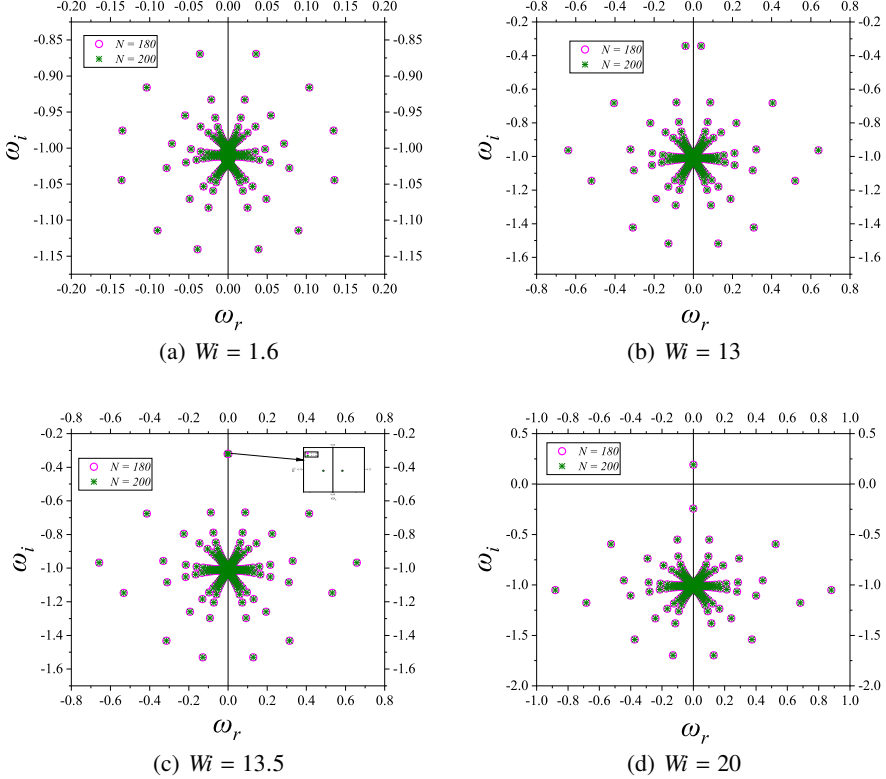


Figure 29: Axisymmetric ($n = 0$) eigenspectra for $\epsilon = 0.1$, $\alpha = 7$, $\beta = 0.98$ at different Wi 's for Dean flow of an Oldroyd-B.

can be attributed to the two- or three-dimensional nature of the disturbance flow field; the original data collapse of [Yamani & McKinley \(2023\)](#); [Tej et al. \(2024\)](#) is expected to hold only for viscometric flows.

Appendix D. Eigenfunctions for viscoelastic Dean flow

In this Appendix, we present the eigenfunctions for the centre mode (CM) and hoop stress modes (HSM1 and HSM2). As discussed earlier, for the eigenspectrum in [Fig. 15](#), the CM instability observed in our work for Dean flow is analogous to the instability reported by [Khalid et al. \(2025\)](#) for channel flow. The eigenfunctions for the CM show strong peaks in $\tilde{\tau}_{\theta\theta}$ and $\tilde{\tau}_{zz}$ near the location of the base-state maximum, a signature that is prominent even in rectilinear channel flow. The eigenfunctions of HSM1 and HSM2, presented in [Figs. 33](#) and [34](#), in contrast, are qualitatively different from those for CM. In fact, the eigenfunctions for HSM2 are closer to those of HSM1, thereby reinforcing that HSM2 is not a continuation of CM.

REFERENCES

- AVGOUSTI, M. & BERIS, A. N. 1993 Nonaxisymmetric modes in viscoelastic Taylor-Couette flow. *Journal of Non-Newtonian Fluid Mechanics* **50** (2), 225 – 251.
- BAI, JUN-JIE, ZHANG, XUAN, WEI, XING, WANG, YU, DU, CHENG, WANG, ZE-JUN, CHEN, MING-LI & WANG, JIAN-

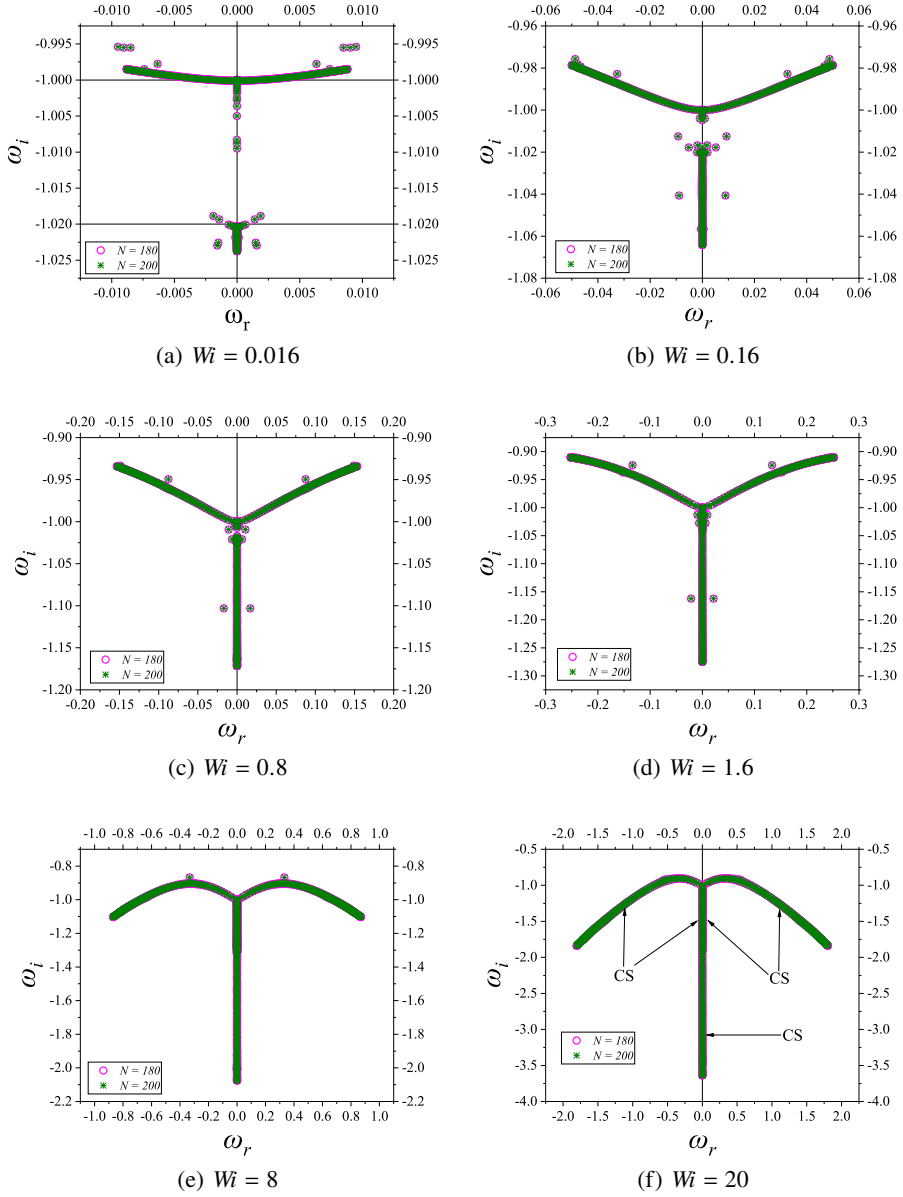


Figure 30: Axisymmetric ($n = 0$) eigenspectra at different Wi 's for Dean flow. Data for $\epsilon = 0.1$, $\alpha = 7$, $\beta = 0.98$, $L = 100$.

HUA 2023 Dean-flow-coupled elasto-inertial focusing accelerates exosome purification to facilitate single vesicle profiling. *Analytical Chemistry* **95** (4), 2523–2531.

BERTOLA, VOLFANGO, MEULENBROEK, BERNARD, WAGNER, CHRISTIAN, STORM, CORNELIS, MOROZOV, ALEXANDER N, VAN SAARLOOS, WIM & BONN, DANIEL 2003 Experimental evidence for an intrinsic route to polymer melt fracture phenomena: A nonlinear instability of viscoelastic Poiseuille flow. *Phys. Rev. Lett.* **90**, 114502.

BIRD, R.B., DOTSON, P.J. & JOHNSON, N.L. 1980 Polymer solution rheology based on a finitely extensible bead—spring chain model. *Journal of Non-Newtonian Fluid Mechanics* **7**, 213 – 235.

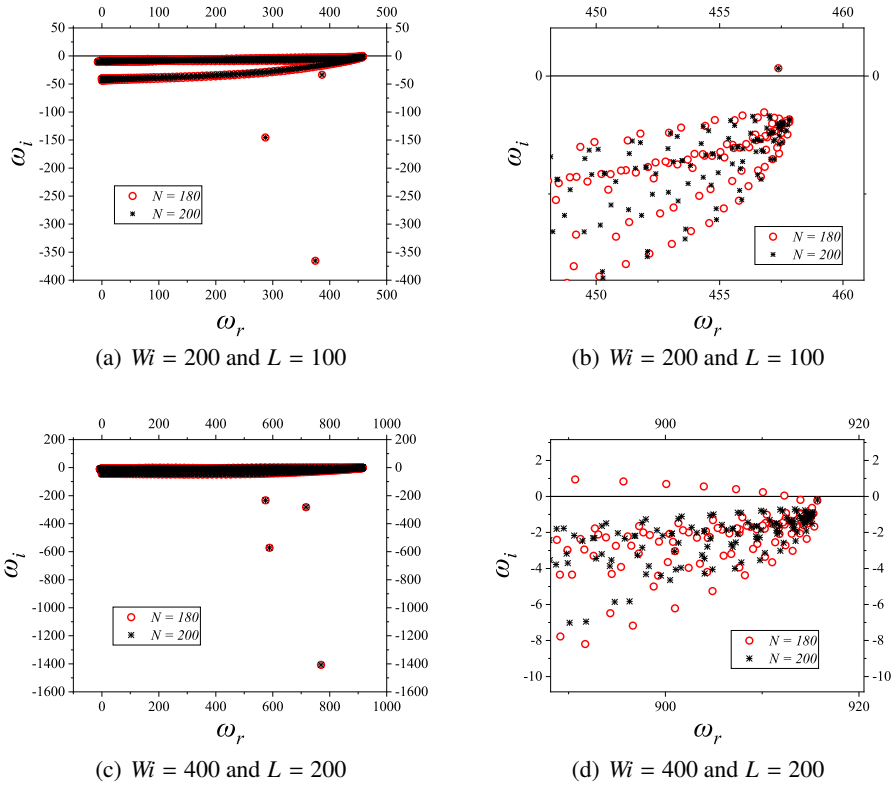


Figure 31: Eigenspectra demonstrating the centre mode in Dean flow of a FENE-P fluid at $Re = 0$, $\alpha = 0.1$, $\beta = 0.98$, $\epsilon = 0.1$, and $n = 16$, for $Wi/L = 2$ but for two (Wi, L) pairs. (a) Full eigenspectrum for the given parameters, and (b) zoomed-in view of (a). Similarly, (c) full eigenspectrum for another set of Wi and L , and (d) zoomed-in view of (c). The eigenspectra obtained for $N = 180$ and 200 show good convergence.

- BISTAGNINO, A., BOFFETTA, G., CELANI, A., MAZZINO, A., PULIAFITO, A. & VERGASSOLA, M. 2007 Nonlinear dynamics of the viscoelastic Kolmogorov flow. *Journal of Fluid Mechanics* **590**, 61–80.
- BOFFETTA, G., CELANI, A., MAZZINO, A., PULIAFITO, A. & VERGASSOLA, M. 2005 The viscoelastic Kolmogorov flow: eddy viscosity and linear stability. *Journal of Fluid Mechanics* **523**, 161–170.
- BUZA, GERGELY, BENEITEZ, MIGUEL, PAGE, JACOB & KERSWELL, RICH R. 2022a Finite-amplitude elastic waves in viscoelastic channel flow from large to zero Reynolds number. *Journal of Fluid Mechanics* **951**, A3.
- BUZA, GERGELY, PAGE, JACOB & KERSWELL, RICH R. 2022b Weakly nonlinear analysis of the viscoelastic instability in channel flow for finite and vanishing Reynolds numbers. *Journal of Fluid Mechanics* **940**, A11.
- BYARS, J. A., OZTEKIN, A., BROWN, R. A. & MCKINLEY, G. H. 1994 Spiral instabilities in the flow of highly elastic fluids between rotating parallel disc. *J. Fluid Mech.* **271**, 173–218.
- CASTILLO SÁNCHEZ, HUGO A., JOVANOVIĆ, MIHAILO R., KUMAR, SATISH, MOROZOV, ALEXANDER, SHANKAR, V., SUBRAMANIAN, GANESH & WILSON, HELEN J. 2022 Understanding viscoelastic flow instabilities: Oldroyd-B and beyond. *Journal of Non-Newtonian Fluid Mechanics* **302**, 104742.
- CHAUDHARY, I., GARG, P., SUBRAMANIAN, G. & SHANKAR, V. 2021 Linear instability of viscoelastic pipe flow. *Journal of Fluid Mechanics* **908**, A11.
- CHEN, DALIN, HUANG, QIANG, NI, ZHONGHUA & XIANG, NAN 2024 Elasto-inertial particle focusing in sinusoidal microfluidic channels. *Electrophoresis* **45**, 2191–2201.
- CHOUERI, GEORGE H., LOPEZ, JOSE M., VARSHNEY, ATUL, SANKAR, SARATH & HOF, BJÖRN 2021 Experimental

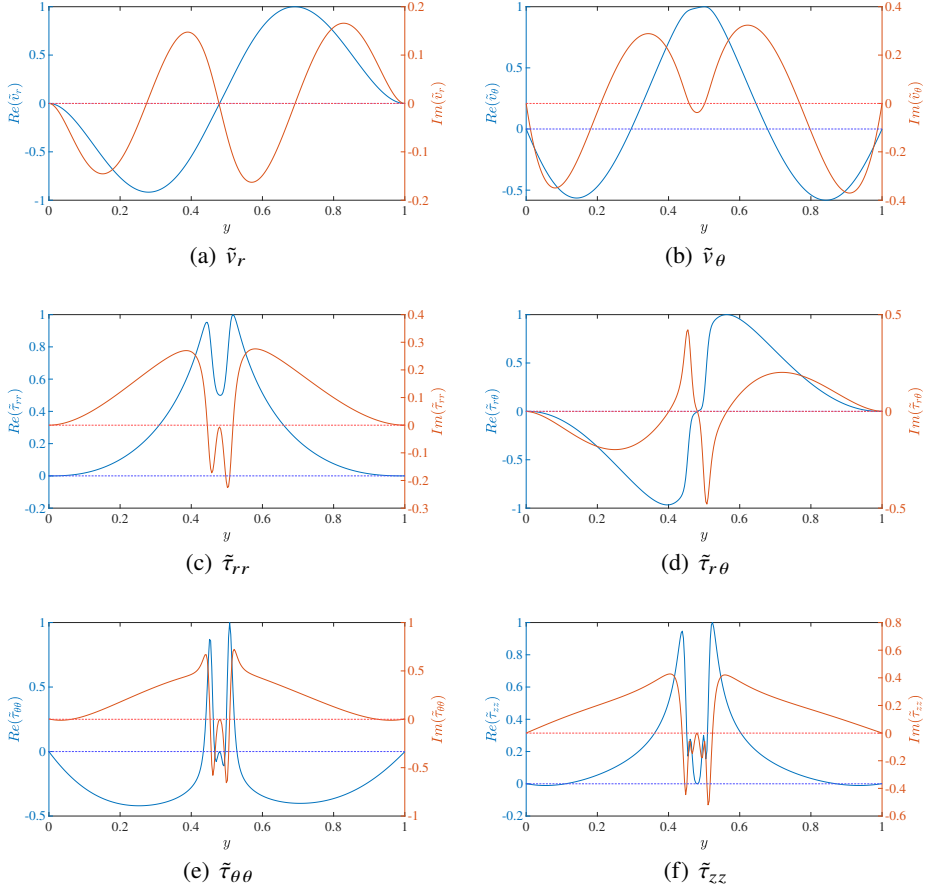


Figure 32: Eigenfunctions for the centre mode ($\omega = 344.258 + 0.00630277i$) in Dean flow of a FENE-P fluid at $Re = 0$, $\alpha = 0$, $\beta = 0.98$, $\epsilon = 0.1$, $L = 100$ and $n = 40$, for $\tilde{Wi} = 60$. The corresponding CM eigenvalue was identified in the eigenspectrum shown previously in Fig. 15. The scales on the left and right y-axes are different, and dotted lines indicate the origins of the respective y-axes.

- observation of the origin and structure of elastoinertial turbulence. *Proceedings of the National Academy of Sciences* **118** (45), e2102350118.
- DATTA, SUJIT S., ARDEKANI, AREZOO M., ARRATIA, PAULO E., BERIS, ANTONY N., BISCHOFBERGER, IRMGARD, MCKINLEY, GARETH H., EGGERS, JENS G., LÓPEZ-AGUILAR, J. ESTEBAN, FIELDING, SUZANNE M., FRISHMAN, ANNA, GRAHAM, MICHAEL D., GUASTO, JEFFREY S., HAWARD, SIMON J., SHEN, AMY Q., HORMOZI, SARAH, MOROZOV, ALEXANDER, POOLE, ROBERT J., SHANKAR, V., SHAQFEH, ERIC S. G., STARK, HOLGER, STEINBERG, VICTOR, SUBRAMANIAN, GANESH & STONE, HOWARD A. 2022 Perspectives on viscoelastic flow instabilities and elastic turbulence. *Phys. Rev. Fluids* **7**, 080701.
- DEAN, W. R. & CHAPMAN, SYDNEY 1928 Fluid motion in a curved channel. *Proceedings of the Royal Society of London. Series A* **121** (787), 402–420.
- DIPRIMA, R. C. 1959 The stability of viscous flow between rotating concentric cylinders with a pressure gradient acting round the cylinders. *Journal of Fluid Mechanics* **6** (3), 462–468.
- DUTCHER, CARL S & MULLER, SUSAN J 2013 Effects of moderate elasticity on the stability of co-and counter-rotating taylor–couette flows. *Journal of Rheology* **57** (3), 791–812.
- GROISMAN, A. & STEINBERG, V. 2001 Efficient mixing at low Reynolds numbers using polymer additives. *Nature* **410**, 905–908.

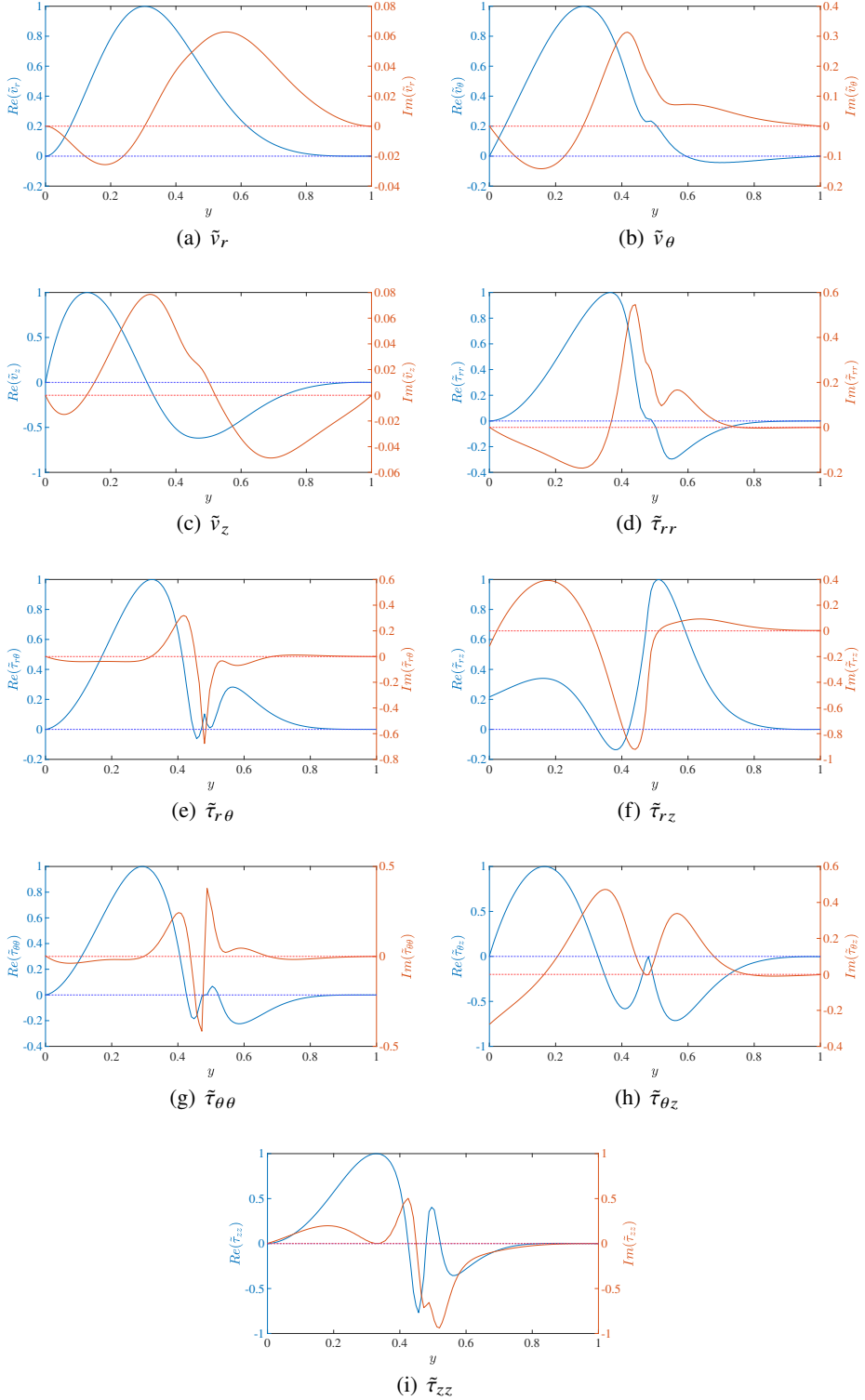


Figure 33: Eigenfunctions for the HSM2 mode ($\omega = 62.786065 + 0.06752153i$) in Dean flow of a FENE-P fluid at $Re = 0$, $\alpha = 7$, $\beta = 0.98$, $\epsilon = 0.1$, $L = 100$, $n = 1$ and $Wi = 400$.

The corresponding HSM2 eigenvalue was identified in the eigenspectrum shown previously in Fig. 21(c). The scales on the left and right y-axes are different, and dotted lines indicate the origins of the respective y-axes.

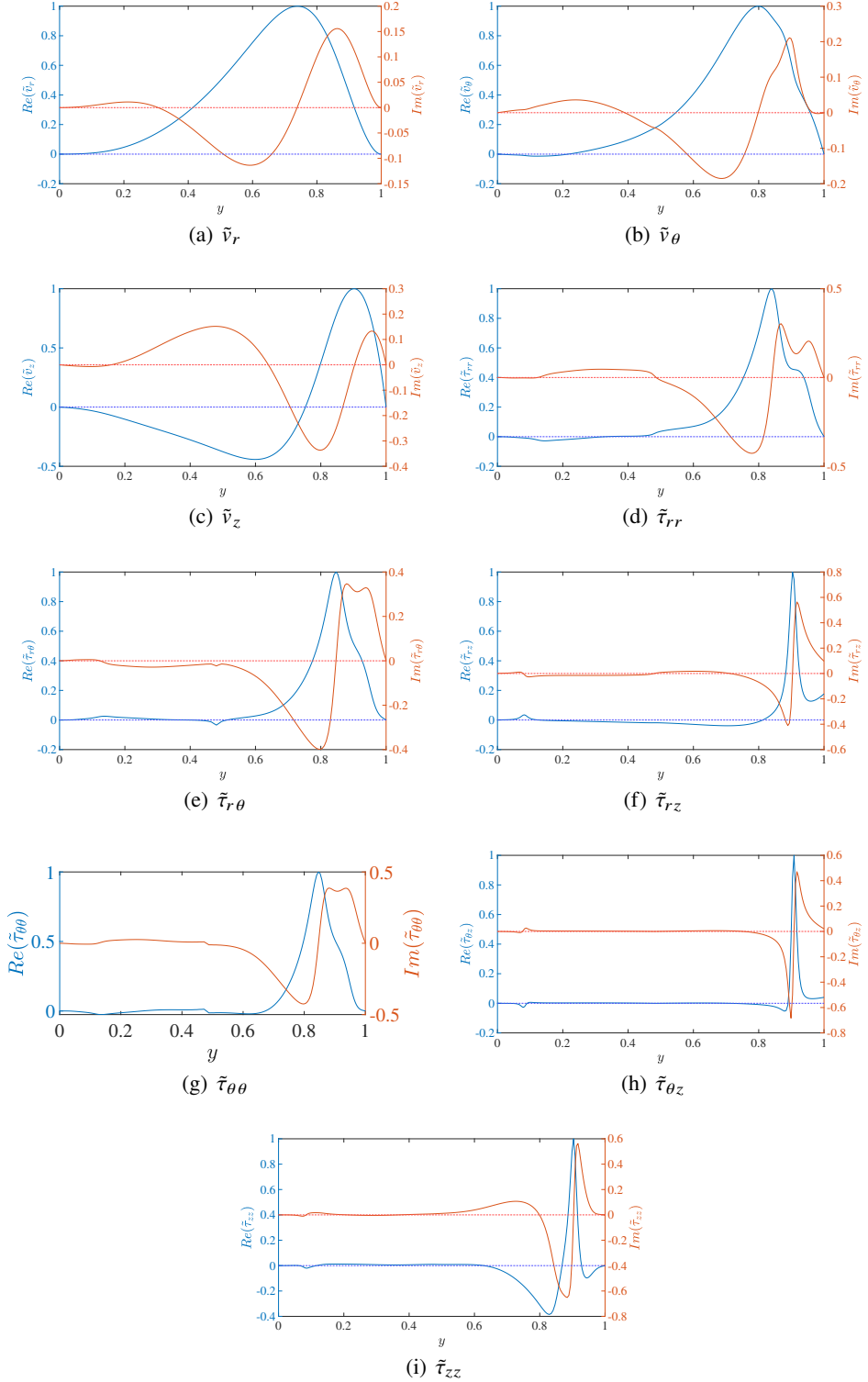


Figure 34: Eigenfunctions for the HSM1 mode ($\omega = 18.2424473 - 6.952907i$) in Dean flow of a FENE-P fluid at $Re = 0$, $\alpha = 7$, $\beta = 0.98$, $\epsilon = 0.1$, $L = 100$ and $n = 1$, for $Wi = 400$. The corresponding HSM1 eigenvalue was identified in the eigenspectrum shown previously in Fig. 21(c). The scales on the left and right y-axes are different, and dotted lines indicate the origins of the respective y-axes.

- GROISMAN, ALEXANDER & STEINBERG, VICTOR 2004 Elastic turbulence in curvilinear flows of polymer solutions. *New J. Phys.* **6**, 29.
- HAWARD, SIMON J., MCKINLEY, GARETH H. & SHEN, AMY Q. 2016 Elastic instabilities in planar elongational flow of monodisperse polymer solutions. *Scientific Reports* **6**, 33029.
- HERBERT, T 1988 Secondary instability of boundary layers. *Annual Review of Fluid Mechanics* **20** (Volume 20, 1988), 487–526.
- HERRCHEN, MARKUS & OTTINGER, HANS CHRISTIAN 1997 A detailed comparison of various FENE dumbbell models. *Journal of Non-Newtonian Fluid Mechanics* **68** (1), 17–42.
- HO, TEH CHUNG & DENN, MORTON M 1977 Stability of plane Poiseuille flow of a highly elastic liquid. *Journal of Non-Newtonian Fluid Mechanics* **3** (2), 179–195.
- JOO, YONG LAK & SHAQFEH, ERIC SG 1991 Viscoelastic Poiseuille flow through a curved channel: A new elastic instability. *Physics of Fluids A: Fluid Dynamics* **3** (9), 2043–2046.
- JOO, YONG LAK & SHAQFEH, ERIC SG 1992 A purely elastic instability in Dean and Taylor–Dean flow. *Physics of Fluids A: Fluid Dynamics* **4** (3), 524–543.
- JOO, YONG LAK & SHAQFEH, ERIC S. G. 1994 Observations of purely elastic instabilities in the Taylor–Dean flow of a booger fluid. *Journal of Fluid Mechanics* **262**, 27–73.
- KERSWELL, RICH R. & PAGE, JACOB 2024 Asymptotics of the centre-mode instability in viscoelastic channel flow: with and without inertia. *Journal of Fluid Mechanics* **991**, A13.
- KHALID, MOHAMMAD, BADONI, AMIT, DUTTA, DEBANJAN, NAIDU, PRAJWAL, SUBRAMANIAN, GANESH & SHANKAR, V. 2025 Role of finite extensibility on the centre-mode instability in viscoelastic channel flow. *Journal of Fluid Mechanics* **1009**, A28.
- KHALID, MOHAMMAD, CHAUDHARY, INDRESH, GARG, PIYUSH, SHANKAR, V. & SUBRAMANIAN, GANESH 2021a The centre-mode instability of viscoelastic plane Poiseuille flow. *Journal of Fluid Mechanics* **915**, A43.
- KHALID, MOHAMMAD, SHANKAR, V. & SUBRAMANIAN, GANESH 2021b Continuous pathway between the elasto-inertial and elastic turbulent states in viscoelastic channel flow. *Phys. Rev. Lett.* **127**, 134502.
- LACASSAGNE, TOM, CAGNEY, NEIL & BALABANI, STAVROULA 2021 Shear-thinning mediation of elasto-inertial Taylor–Couette flow. *Journal of Fluid Mechanics* **915**, A91.
- LARSON, R. G. 1988 *Constitutive Equations for Polymer Melts and Solutions*. Butterworths.
- LARSON, R. G., SHAQFEH, ERIC S. G. & MULLER, S. J. 1990 A purely elastic instability in Taylor–Couette flow. *Journal of Fluid Mechanics* **218**, 573–600.
- LEWY, THEO & KERSWELL, RICH R 2025 Revisiting two-dimensional viscoelastic Kolmogorov flow: a centre-mode-driven transition. *Journal of Fluid Mechanics* **1007**, A55.
- MCKINLEY, GARETH H., BYARS, JEFFREY A., BROWN, ROBERT A. & ARMSTRONG, ROBERT C. 1991 Observations on the elastic instability in cone-and-plate and parallel-plate flows of a polyisobutylene booger fluid. *Journal of Non-Newtonian Fluid Mechanics* **40** (2), 201 – 229.
- MCKINLEY, G. H., OZTEKIN, A., BYARS, J. A. & BROWN, R. A. 1995 Self-similar spiral instabilities in elastic flows between a cone and a plate. *J. Fluid Mech.* **285**, 123–164.
- MCKINLEY, GARETH H., PAKDEL, PEYMAN & OZTEKIN, ALPARSLAN 1996 Rheological and geometric scaling of purely elastic flow instabilities. *Journal of Non-Newtonian Fluid Mechanics* **67**, 19–47.
- MOHANTY, PRATYUSH KUMAR, TEJ, P. S. D. SURYA PHANI, SUBRAMANIAN, GANESH & SHANKAR, V. 2025 Nature of continuous spectra in wall-bounded shearing flows of FENE-P fluids, arXiv: 2512.05787.
- MORE, RISHABH V, PATTERSON, R, PASHKOVSKI, E & MCKINLEY, GARETH H 2024 Elasto-inertial instability in torsional flows of shear-thinning viscoelastic fluids. *Journal of Fluid Mechanics* **985**, A37.
- MOROZOV, A. N. & VAN SAARLOOS, W. 2005a Subcritical finite-amplitude solutions for plane Couette flow of viscoelastic fluids. *Phys. Rev. Lett.* **95**, 024501.
- MOROZOV, ALEXANDER N. & VAN SAARLOOS, WIM 2005b Subcritical instabilities in plane Couette flow of visco-elastic fluids. In *IUTAM Symposium on Laminar-Turbulent Transition and Finite Amplitude Solutions* (ed. Tom Mullin & Rich Kerswell), *Fluid Mechanics and its Applications*, vol. 77, pp. 313–330. Springer Netherlands.
- MOROZOV, A. N. & VAN SAARLOOS, W. 2007 An introductory essay on subcritical instabilities and the transition to turbulence in viscoelastic parallel shear flows. *Phys. Rep.* **447**, 112–143.
- MOROZOV, A. N. & VAN SAARLOOS, W. 2019 Subcritical instabilities in plane Poiseuille flow of an Oldroyd-B fluid. *J. Stat. Phys.* **175**, 554–577.
- NEELAMEGAM, R., SHANKAR, V. & DAS, DEBOPAM 2013 Suppression of purely elastic instabilities in the torsional flow of viscoelastic fluid past a soft solid. *Physics of Fluids* **25** (12), 124102.

- NIKDOOST, ARSALAN & REZAI, POUYA 2020 Dean flow velocity of viscoelastic fluids in curved microchannels. *AIP Advances* **10** (8), 085015.
- OZTEKIN, ALPARSLAN, BROWN, ROBERT A. & MCKINLEY, GARETH H. 1994 Quantitative prediction of the viscoelastic instability in cone-and-plate flow of a Boger fluid using a multi-mode Giesekus model. *Journal of Non-Newtonian Fluid Mechanics* **54**, 351–377.
- PAGE, J., DUBIEF, Y. & KERSWELL, R. R. 2020 Exact travelling wave solutions in viscoelastic channel flow. *Phys. Rev. Lett.* **125**, 154501.
- PAKDEL, PEYMAN & MCKINLEY, GARETH H. 1996 Elastic instability and curved streamlines. *Phys. Rev. Lett.* **77**, 2459–2462.
- PAN, L., MOROZOV, A., WAGNER, C. & ARRATIA, P. E. 2013 Nonlinear elastic instability in channel flows at low Reynolds numbers. *Phys. Rev. Lett.* **110**, 174502.
- PRIYADARSHI, MAMTA, SRITA, KOPPARTHI V., BHASKAR, V. V. K. N. SAI, KHALID, MOHAMMAD, SUBRAMANIAN, GANESH & SHANKAR, V. 2023 A new elastic instability in gravity-driven viscoelastic film flow. *Physics of Fluids* **35**, 073104.
- RAMANAN, V. V., KUMAR, K. A. & GRAHAM, M. D. 1999 Stability of viscoelastic shear flows subjected to steady or oscillatory transverse flow. *Journal of Fluid Mechanics* **379**, 255–277.
- ROY, ANUBHAB, GARG, PIYUSH, REDDY, JUMPAL SHASHIKIRAN & SUBRAMANIAN, GANESH 2022 Inertio-elastic instability of a vortex column. *Journal of Fluid Mechanics* **937**, A27.
- SAMANTA, D., DUBIEF, Y., HOLZNER, M., SCHÄFER, C., MOROZOV, A. N., WAGNER, C. & HOF, B. 2013 Elasto-inertial turbulence. *Proceedings of the National Academy of Sciences* **110** (26), 10557–10562.
- SCHAEFER, CHRISTOF, MOROZOV, ALEXANDER & WAGNER, CHRISTIAN 2018 Geometric scaling of elastic instabilities in the Taylor–Couette geometry: a theoretical, experimental and numerical study. *Journal of Non-Newtonian Fluid Mechanics* **259**, 78–90.
- SCHMID, PETER J. & HENNINGSON, DAN S. 2001 *Stability and Transition in Shear Flows*, Applied Mathematical Sciences, vol. 142. New York, NY: Springer.
- SHAKERI, PEGAH, JUNG, MICHAEL & SEEMANN, RALF 2021 Effect of elastic instability on mobilization of capillary entrapments. *Physics of Fluids* **33** (11), 113102.
- SHAQFEH, ERIC S.G. & KHOMAMI, BAMIN 2021 The Oldroyd-B fluid in elastic instabilities, turbulence and particle suspensions. *Journal of Non-Newtonian Fluid Mechanics* **298**, 104672.
- SHAQFEH, E. S. G. 1996 Purely elastic instabilities in viscometric flows. *Annu. Rev. Fluid Mech.* **28**, 129–185.
- STEINBERG, VICTOR 2021 Elastic turbulence: An experimental view on inertialess random flow. *Annual Review of Fluid Mechanics* **53** (1), 27–58.
- TEJ, P.S.D. SURYA PHANI, MOHANTY, PRATYUSH KUMAR & SHANKAR, V. 2024 Master curves for unidirectional flows of FENE-P fluids in rectilinear and curvilinear geometries. *Journal of Non-Newtonian Fluid Mechanics* **334**, 105332.
- TREFETHEN, L. N. 2000 *Spectral Methods in MATLAB*. Philadelphia: SIAM.
- WEIDEMAN, J ANDRE & REDDY, SATISH C 2000 A MATLAB differentiation matrix suite. *ACM Trans. Math. Softw.* **26**, 465–519.
- WILSON, H J, RENARDY, M & RENARDY, Y Y 1999 Structure of the spectrum in zero Reynolds number shear flow of the UCM and Oldroyd-B liquids. *Journal of Non-Newtonian Fluid Mechanics* **80** (2-3), 251–268.
- YADAV, SHAILENDRA KUMAR, SUBRAMANIAN, GANESH & SHANKAR, V. 2024 Elastic instability in a family of rectilinear viscoelastic channel flows devoid of centerline symmetry. *Phys. Rev. Fluids* **9**, 013301.
- YAMANI, SAMI & MCKINLEY, GARETH H. 2023 Master curves for FENE-P fluids in steady shear flow. *Journal of Non-Newtonian Fluid Mechanics* **313**, 104944.
- ZHANG, YI-BAO, LI, LU, FAN, YANING, SU, JINGHONG, XI, HENG-DONG & SUN, CHAO 2025 Experimental evidence for the continuous transition between elastic and elastoinertial turbulence. *Proceedings of the National Academy of Sciences* **122** (38), e2505007122.